Environmental instability prior to end-Permian mass extinction reflected in biotic and facies changes on shallow carbonate platforms of the Nanpanjiang Basin (South China)

Li Tian[a,b*], Jinnan Tong[a*], Yifan Xiao[a], Michael J. Benton[b], Huyue Song[a], Haijun Song[a], Lei Liang[a], Kui Wu[a], Daoliang Chu[a], and Thomas J. Algeo[a,c,d]

[a] *State Key Laboratory of Biogeology and Environmental Geology, China University of Geosciences, Wuhan, 430074, China*

[b] *School of Earth Sciences, University of Bristol, BSB 1 RJ, UK*

[c] *Department of Geology, University of Cincinnati, Cincinnati, OH 45221-0013, U.S.A.*

[d] *State Key Laboratory of Geological Processes and Mineral Resources, China University of Geosciences, Wuhan 430074, China*

*Corresponding authors: tianlibgeg@163.com (L. Tian); jntong@cug.edu.cn (J. Tong)

Abstract

Shallow carbonate platforms exhibit major changes in faunal composition and facies types during the latest Permian and earliest Triassic. Although the microbialites that developed following the latest Permian mass extinction (LPME) have attracted wide attention, temporal variations in shallow-platform facies and faunas prior to the LPME have been less thoroughly studied. Here, we analyze diversity patterns and variation in skeletal composition in three Upper Permian sections from isolated carbonate platforms of the Nanpanjiang Basin. In addition to the well-known transition from fossil-rich Upper Permian limestones to fossil-poor Permian-Triassic boundary (PTB) microbialites,

these sections exhibit several distinct changes that predate the LPME. First, foram faunas show a shift from non-fusulinid-dominated to fusulinid-dominated communities in the <1-m interval below the LPME horizon of each section, reflecting a shallowing trend over ~20–30 kyr preceding the mass extinction. Second, a "foram gap" and concurrent "detrital event" are observed below the LPME in all three sections, recording a rapid influx of detrital siliciclastics that predated the mass extinction by <60 kyr. These features reflect a degree of marine environmental instability prior to the end-Permian mass extinction. The sudden influx of siliciclastics may represent an early perturbation to terrestrial ecosystems linked to incipient Siberian Traps magmatism, resulting in secondary effects in marine environments through increased sediment yields.

Keywords: microbialite; bioclastic limestone; microfacies; foraminifera; Early Triassic; Late Permian

1. Introduction

As the largest extinction event of the Phanerozoic, the latest Permian mass extinction (LPME) at 252.2 Ma (Shen et al., 2011; Burgess et al., 2014) eliminated over 90 % of species and 79 % of genera of marine invertebrates (Raup, 1979; Shen et al., 2011; Payne and Clapham, 2012; Song-HJ et al., 2013). This biotic crisis led to the collapse of metazoan reefs, triggered the reappearance of anachronistic carbonate facies such as microbialites, and fundamentally altered the structure of marine ecosystems (Flügel, 2002; Bambach, 2002; Weidlich et al., 2003; Payne et al., 2004; Knoll et al., 2007; Bottjer et al., 2008; Algeo et al., 2011; Kershaw et al., 2012a; Tian et al., 2015a, 2015b). It also initiated a ~5-Myr-long interval of major perturbations to the global carbon and sulfur cycles, as recorded in large (to 10 ‰) excursions in carbonate $\delta^{13}C$ and sulfate $\delta^{34}S$ (Payne et al., 2004; Xie et

al., 2010; Song-HY et al., 2014a).

Skeletal abundance declined sharply during the end-Permian crisis, reflecting ecological and oceanographic effects (Knoll et al., 1996, 2007; Payne et al., 2006, 2007; Knoll and Fischer, 2011). Knoll et al. (1996) analyzed long-term secular variation in the degree of calcification of marine invertebrate taxa, showing major declines at both the Middle-Late Permian and Permian-Triassic boundaries. Although taxonomic diversity during the Late Permian was lower than in the Middle Permian, skeletal carbonates were still major components of shallow-marine facies, comprising 30–60 % of carbonate platform interiors, but following the LPME they were reduced to just < 10 % of these facies (Payne et al., 2006; Wang et al., 2009; Tian et al., 2014a).

The end-Permian mass extinction occurred in two stages, as shown by studies at Meishan D (the global stratotype section and point, GSSP, of the PTB) and other sections. At Meishan D, the first extinction episode commenced at the top of the latest Permian *Clarkina yini* conodont Zone and the second episode is in the lower part of the earliest Triassic *Isarcicella isarcica* Zone (Shen et al., 2011; Song-HJ et al., 2013), representing a temporal offset of ~61 (± 48) kyr per recent radiometric dating results (Burgess et al., 2014). Each of these extinction episodes was accompanied by major changes in environmental conditions (Xie et al., 2007; Song-HJ et al., 2009a, 2013, 2014). The question of whether marine environmental conditions prior to the first extinction episode were entirely stable or whether there is evidence of "precursor" perturbations has only begun to be addressed in recent studies, some of which have inferred a limited expansion of oceanic euxinia and increased terrestrial inputs (e.g., Li et al., 2016; Dudás et al., 2017; Elrick et al., 2017; Zhang et al., 2018) as well as impacts on deep-water faunas such as radiolarians (Feng and Algeo, 2014) prior to the LPME.

In contrast to slope sections such as Meishan, most shallow-marine shelf and platform sections

67 record only a single extinction event during the Permian-Triassic (P-Tr) transition (e.g., Bulla:
68 Farageboli et al., 2007; Gorjan et al., 2007; Yangou: Tian et al., 2014a). These sections are
69 commonly dominated by microbial facies immediately above the LPME horizon, known as
70 Permian-Triassic boundary microbialites (PTBM), whose depositional conditions and community
71 structure have been well-studied (Ezaki et al., 2003, 2008; Lehrmann et al., 2003, 2007; Baud et al.,
72 2005; Pruss et al., 2006; Wang et al., 2009; Song-HJ et al., 2009b; Kershaw et al., 2009, 2011, 2012a;
73 Yang et al., 2011). These sections commonly contain evidence of major environmental changes
74 associated with the LPME (e.g., sea-level fluctuations and ocean acidification) that is not found in
75 deeper settings (Payne et al., 2007; Wignall et al., 2009; Kershaw et al., 2012a; Yin et al., 2014).

76 Far less attention has been paid to invertebrate community and carbonate microfacies changes in
77 shallow-marine shelf and platform settings before the LPME. The Nanpanjiang Basin in the
78 southwestern South China Craton contains dozens of continuous carbonate PTB sections that are
79 well exposed, facilitating investigation of biotic and environmental changes on shallow-marine
80 platforms (Lehrmann et al., 2003, 2007; Enos et al., 2006; Algeo et al., 2007). The primary goal of
81 the present study is to understand the nature of the P-Tr transition in shallow carbonate platform
82 settings through analysis of skeletal variations, microfacies changes, before and after the extinction.
83 To this end, we examined foraminiferal distributions and quantified the skeletal composition of
84 carbonate rock from three shallow carbonate platform sections (Wengna, Taiping, and Lung Cam) in
85 the Nanpanjiang Basin. We use these paleontological and sedimentary data to establish variations in
86 biodiversity and paleocommunity patterns between shallow carbonate platforms and other types of
87 contemporaneous depositional settings globally. This analysis provides new insights into the timing
88 and nature of pre-LPME biotic and environmental changes in shallow-marine platform settings.

2. Geological setting and methods

The Nanpanjiang Basin was located on the southeastern paleomargin of the South China Craton at a low Northern Hemisphere paleolatitude during the P-Tr transition (Fig. 1A; note that this craton was rotated ~80° counterclockwise in the P-Tr relative to its modern orientation). Deep-water areas of the Nanpanjiang Basin accumulated mainly thin-bedded muddy limestones, radiolarian cherts, and fine-grained siliciclastics. Scattered across the Nanpanjiang Basin were a number of isolated shallow carbonate platforms, including the Great Bank of Guizhou (GBG) and the Pingguo, Chongzuo, Debao, and Jinxi platforms (Fig. 1B; Lehrmann et al., 1998; Enos et al., 2006). These were low-relief platforms with gentle slopes during the P-Tr transition, although they subsequently grew to immense sizes (100s of meters in height) with steep slopes during the Triassic Period. The platforms exhibit generally similar macrofacies successions through the P-Tr transition (i.e., uppermost Permian bioclastic limestones replaced by PTBMs) (Lehrmann et al., 2003).

The Wengna section is exposed in a cornfield close to Wengna Village (25°33’05”N; 106°41’10”E), Luodian County, Guizhou Province. It was located on the northern margin of the Great Bank of Guizhou at inferred water depths of ~10–30 m (Fig. 1B). It consists of bioclastic limestone of the Upper Permian Wujiaping Formation and overlying microbialites of the Lower Triassic Daye Formation (Fig. 2; Lehrmann, 1999; Lehrmann et al., 2001; Wang et al., 2005). The PTB, indicated by the first occurrence of *Hindeodus parvus*, is at the base of the microbialites (Jiang et al., 2014). Placement of the LPME is facilitated by the carbonate $\delta^{13}C$ profile, which exhibits a 1 ‰ negative shift ~55 cm below the PTB (Song-HY et al., 2014b). Two possible erosion surfaces (Fig. 2A, C) were noted in outcrop: the upper one located at the lithologic contact between

111 Wujiaping bioclastic limestones and Daye microbialites (called the “basal PTBM diastem” in this
112 study; see below), and the lower one associated with a 2-cm-thick muddy limestone layer located 40
113 cm below this contact (called the “uppermost Permian diastem”).

114 The Taiping section is located 500 m northeast of Taiping Town, Pingguo County, Guangxi
115 Province (23°30’00”N; 107°31’20”E). It was deposited in the interior of the Pingguo Platform at
116 inferred water depths of ~10–30 m (Fig. 1B; water depths may have been greater in the early to
117 middle Late Permian as suggested by chert interbeds in the lower Heshan Formation). It consists of
118 medium-bedded bioclastic limestone of the Upper Permian Heshan Formation, overlain by
119 microbialites of the Lower Triassic Majiaoling Formation (Fig. 3B). The PTB is located at the base
120 of the microbialites based on the first occurrence datum of *H. parvus* (unpublished data from Kui
121 Wu). Placement of the LPME is facilitated by the carbonate $\delta^{13}C$ profile, in which a decline of
122 ~0.6 ‰ began ~2.4 m below the formation contact (Fig. 4; Luo et al., 2011). Two possible erosion
123 surfaces were noted in outcrop: the lower one located at the lithologic contact between Heshan
124 bioclastic limestones and Majiaoling microbialites (“basal PTBM diastem”; see below), and the
125 upper one located along a stylolite 2 cm above this contact (“lowermost Triassic diastem”; Fig. 3B).

126 The Lung Cam section is located near Lung Cam village, Ha Giang Province, Vietnam, about 10
127 km south of the Chinese border (23°14’30”N; 105°13’20”E). It was deposited on the southern part of
128 the Jinxi Platform at inferred water depths of ~10–30 m (Fig. 1B). It consists of bioclastic limestones
129 of the Upper Permian Dong Dang Formation overlain by microbialites and micritic limestones of the
130 Lower Triassic Hong Ngai Formation. Although *H. parvus* has not been reported from Lung Cam or
131 the nearby Nhi Tao section to date (Algeo et al., 2007; Son et al., 2007), the PTB is likely to be
132 located at or close to the base of the microbialite based on analogy with similar sections in South

China (such as Wengna and Taiping above). Approximate placement of the LPME is facilitated by the carbonate $\delta^{13}C$ profile, which exhibits a gradual decrease beginning ~1.2 m below the formation contact, followed by an abrupt shift at the formation contact (Fig. 4; Son et al., 2007). The presence of erosional surface(s) within the Lung Cam section has not been investigated in the field to date.

The nature of the contact between the PTBM and underlying Upper Permian bioclastic limestones varies among these three sections. At Taiping, the lithologic contact is expressed as dark gray microbialites above a flat surface at the top of light gray bioclastic limestones (red arrow, Fig. 3B), although a stylolitized horizon is present two centimeters above this contact (blue arrow, Fig. 3B). A similar arrangement is present in the Laibing section on the Great Bank of Guizhou (Payne et al., 2007). At Wengna, the lithologic contact is expressed as dark-colored microbialites above a gently undulating (~2-cm relief) surface at the top of light gray bioclastic limestones (Fig. 2A, C). The diastem at base of PTBMs shows features that may be consistent with a hiatus (time gap) (Kershaw et al., 2009, 2012a; Yin et al., 2014; Yang et al., 2011). The contact is commonly stylolitized, as at Yudongzi and Dongwan (Kershaw et al., 2012a, 2012b), making interpretation of original depositional relationships difficult. Yin et al. (2014) employed high-resolution conodont biostratigraphic correlation to calibrate the latest Permian hiatus in South China, although uncertainties remain in areas of microbialite development owing to insecure placement of the P-Tr boundary. Earlier studies reported the first occurrence of *H. parvus* in the middle of the microbialite facies (Wang et al., 2005; Chen et al., 2009a), which implied that the lower microbialite was of latest Changhsingian age and, thus, that these sections might be stratigraphically complete (i.e., without a diastem at the lithologic contact at the base of the microbialite). However, recent studies have identified *H. parvus* from close to the base of the microbialites at Dajiang and Cili, implying that the

155 microbialite is mostly or entirely of early Griesbachian age, and, therefore, that a diastem is present
156 at the base of the microbialite ("basal PTBM diastem") (Jiang et al., 2014; Wang et al., 2015). The
157 present study sections (Wengna and Taiping) show the same pattern (see above). Although initiation
158 of PTBM growth may have been diachronous globally (Kershaw et al., 2012a), the available
159 evidence suggests that their bases are approximately correlative across the Nanpanjiang Basin (Fig.
160 4).

161 In each study section, samples were collected at regular intervals through the P-Tr transition in
162 order to generate thin sections. A total of 20, 29, and 23 thin sections were made for the Wengna,
163 Taiping, and Lung Cam sections, respectively. Note that the formation contact intervals of the
164 Uppermost Permian bioclastic limestone with the bases of PTBMs had been continuously sampled (<
165 2cm) whilst other intervals were sampled with larger spaces (sampling locations are marked along
166 the lithology columns). Although the raw sampling spaces varied, they are comparable temporally as
167 we collected similar numbers of samples in equivalent time intervals (Fig. 4). In these thin sections,
168 thousands of individual foraminifers were observed and identified. Microfacies analysis was
169 conducted following the procedures and revised standard microfacies classification of Flügel (2004).
170 In addition, carbonate components were quantified by point-counting, with 100 points counted per
171 thin section using a 10 x 10 grid with nodes 1 mm apart. Fossil frequency was calculated as fossil
172 count / total count × 100 %.

173

174 **3. Results**

175 *3.1. Wengna section*

176 A total of 34 species of foraminifers belonging to 27 genera were identified in the Wengna

177 section (Fig. 5), including *Palaeofusulina minima*, *Palaeofusulina sinensis*, *Sphaerulina* sp.,
178 *Nankinella* spp., *Paraeichelina* sp., *Palaeotextularia* spp., *Reichelina* spp. (Fig. 6), and eight
179 fusulinid species. This assemblage is dominated by *Palaeofusulina* spp., *Pachyphloia* spp., and
180 *Nodosinelloides* spp. The typical Permian fauna, represented by *Palaeofusulina sinensis*, *Nankinella*
181 spp., and *Pachyphloia robusta*, did not reappear after their disappearance at the LPME, representing
182 the major extinction horizon in the Wengna section (Fig. 5). The only foram taxa that survived into
183 the microbialite interval were *Frondina permica*, *Nodosinelloides aequiampla*, *Geinitzina uralica*,
184 and *Rectocornuspira kalhori*. The muddy limestone bed located 40 cm below the lithologic contact
185 ("late Permian diastem") contains no forams ("foram gap"; Fig. 5), although most species reappear in
186 the immediately overlying beds, indicating a local facies-controlled disappearance rather than an
187 extinction event.

188 Four microfacies types were recognized at Wengna: (1) MF1: algal-foraminiferal
189 packstone-grainstone; (2) MF2: dolomitized wackestone; (3) MF3: algal-foraminiferal grainstone;
190 and (4) MF4: dolomitized gastropod wackestone (Fig. 5). MF1 and MF3 are characterized by diverse
191 bioclasts, especially algal and foraminiferal grains. MF1 differs from MF3 by the presence of micrite
192 in the matrix. MF2 and MF4 are characterized by extensive dolomitization. Whereas MF2 is largely
193 non-fossiliferous and contains only a few fossil fragments and ichnofossils, MF4 contains abundant
194 gastropods and ostracods. Irregular sparry mosaics are present in MF4 due to inhomogeneous
195 dolomitization. Additionally, potential cyanobacterial fossils were observed in MF4 (Fig. 5E). These
196 features observed in MF4 (non-fossiliferous micrite dominated, irregular sparry mosaics associated
197 as well as layers of gastropods and ostracods interbedded) are typical of calcimicrobial-related
198 structures in microbialites (Lehrmann, 1999; Wang et al., 2005). All these observations suggest open

to slightly restricted shallow-marine platform environments.

3.2. Taiping section

A total of 27 species of foraminifers belonging to 22 genera were identified in the Taiping section (Fig. 7), including 2 genera of fusulinids, *Nankinella* and *Reichelina* (Fig. 8). This assemblage is characterized by high abundances of *Nankinella* sp. and *Pachyphloia* spp. All species except *Tolypammina* sp. are found in the Upper Permian, whereas only *Rectocornuspira kalhori*, *Globivalvulina bulloides*, *Hemigordius* spp., and *Tolypammina* sp. were found in the Lower Triassic microbialites. Associated with the lithological transition from bioclastic limestone to microbialites, biodiversity declined abruptly, reflecting the position of the LPME at Taiping (Fig. 7). Forams disappear from a sandy limestone layer bearing detrital quartz and feldspar that is located 2.4–2.3 m below the LPME ("foram gap"; Fig. 7), but the re-appearance of most species in the immediately overlying beds indicates a local facies-controlled disappearance rather than an extinction event.

Four microfacies types were recognized at Taiping: (1) MF1: foraminiferal packstone; (2) MF2: algal-foraminiferal packstone; (3) MF3: sandy carbonate mudstone; and (4) MF4: dolomitized wackestone (Fig. 7). MF2 is characterized by greater fossil diversity and a higher abundance of algae than MF1, implying an open-marine platform environment. MF3 contains abundant quartz and feldspar grains, representing strong detrital input. MF4 is marked by a low abundance and low diversity of fossil fragments (dominantly ostracods), although many fossil fragments cannot be identified because of dolomitization. Dominance of ostracods and a dark micritic matrix indicate a relatively restricted platform environment.

221 *3.3. Lung Cam section*

222 A total of 17 species of foraminifers belonging to 17 genera were identified in the uppermost
223 Permian of the Lung Cam section (Fig. 9), including two genera of fusulinids (*Nankinella* spp. and
224 *Reichelina* sp.; Fig. 10). *Nankinella* spp. and *Glomomidiella nestellorum* are the most abundant
225 species of this assemblage. The basal Triassic microbialites yielded no foram specimens. However,
226 foram range data for Lung Cam are likely to be incomplete owing to relatively poorer fossil
227 preservation than at Wengna and Taiping because of extensive micritization of bioclasts, making it
228 impossible to identify many specimens to the genus or species level. A "foram gap" similar to those
229 at Wengna and Taiping is present at Lung Cam about 15 cm below the lithologic contact.

230 Four microfacies types were recognized at Lung Cam: (1) MF1: Bivalve-ostracod packstone; (2)
231 MF2: algal-foraminiferal packstone-grainstone; (3) MF3: clast-bearing mudstone; and (4) MF 4:
232 dolomitized ostracod wackestone (Fig. 9). MF1 samples have a dark micritic matrix, suggesting a
233 relative deeper environment. MF2 samples are characterized by diverse fossil types, indicating an
234 open-platform environment. The clast-bearing mudstone of MF3 contains mica and black clasts and
235 lacks fossils, indicating increased siliciclastic input. MF4 samples contain mainly ostracods,
236 suggesting a restricted inner-platform environment, which is consistent with their stronger
237 dolomitization.

238

239 *3.4. Permian-Triassic boundary microbialites (PTBM)*

240 Each of the three study sections contains the PTBM, which represent an "anachronistic facies"
241 (Baud et al., 2007) that developed widely in the aftermath of PTB crisis and that can provide insights
242 into paleoenvironmental conditions following the extinction (Ezaki et al., 2003, 2008; Lehrmann et

al., 2003, 2007; Pruss et al., 2006; Kershaw et al., 2007, 2012a; Yang et al., 2011).

At Wengna, the microbialite is gray, digitate and thrombolitic in structure (Fig. 2). It is assigned to MF4 (dolomitized gastropod wackestone). In the basal PTBM (76–86 cm, Fig. 5), bioclasts consist of 1–2 % gastropods and <10 % ostracods, microconchids, and small foraminifers such as *Rectocornuspira kalhori* (Fig. 6A, 6B). In the upper PTBM (86–100 cm, Fig. 5), total fossil frequency increased to 20–30 %, with larger numbers of gastropods in the interbeds but no significant changes in the abundances of foraminifers and ostracods (Fig. 5). Several more foraminiferal taxa, including *Frondina permica*, *Nodosinelloides aequiampla*, and *Geinitzina uralica*, are found in the upper PTBM although their abundances are low (0–4 %). Two probable calcified microbes (*Renalcis*-like and coccoidal forms) and a few small (200–600 μm) microcochids, identified by their spiral tube (longitudinal view) or donut-shape (transverse view), have micritic wall structures. The *Renalcis*-like microbe is characterized by a chambered structure, whereas the coccoidal microbe consists of small micritic spherules organized in clots/clusters and surrounded by sparry matrix (Figs. 5E, 11E).

At Taiping, the microbialites are dark thrombolites consisting of a digitate micritic framework enclosed in sparry cement (Fig. 3C). Total fossil abundances were 8–20 %, with dominance of ostracods in both the shelly layers and the micritic matrix. The few foraminifers were preserved in the micritic matrix. In contrast, two probable calcified microbes (*Renalcis*-like and coccoidal forms) were preserved within areas of sparry cements (Fig. 7F), although they were enclosed by chambered belts (Fig. 11F) and dark micritic clots (Fig. 11E), respectively.

At Lung Cam, limited sampling of the PTBM obviates a comprehensive description. We noted that a sample from the basal Hong Ngai Formation belonging to MF4 (dolomitized ostracod

265 wackestone) is characterized by occurrences of coccoidal micritic clots and abundant bioclasts
266 (dominated by 20 % ostracods) (Fig. 9). The similarity of microfacies types and skeletal
267 compositions with the Wengna and Taiping sections suggests that the PTBM at Lung Cam was also a
268 thrombolite.

269

270 **4. Discussion**

271 *4.1. Secular variation in fossil assemblages and extinction events*

272 The stratigraphic distributions of fossil taxa in the Wengna and Taiping sections exhibit similar
273 patterns, with the following characteristics: (1) bioclasts in the pre-LPME Upper Permian are
274 dominated by algae and foraminifers; (2) the Lower Triassic microbialites contain only ostracods,
275 gastropods, microconchids, and rare foraminifers; and (3) the abundant and diverse Upper Permian
276 foraminifer assemblages were replaced by sparse, low-diversity assemblages in the Lower Triassic,
277 showing that forams experienced the same abrupt extinction at the LPME as marine invertebrate taxa
278 (Figs. 5, 7). The Lung Cam section displays some unique features that distinguish it from the other
279 two study sections: (1) the Upper Permian contains abundant molluscs and ostracods in addition to
280 foraminifers, and algae are rarer; (2) ostracods comprise up to 20 % of the Lower Triassic
281 microbialite facies, but no other bioclast type was found (note: only one sample was analyzed from
282 the microbialite facies at Lung Cam, so this result may not be fully representative); (3) foraminifera
283 exhibit a stepwise disappearance pattern in the uppermost Permian, with no obvious single extinction
284 horizon (Fig. 9). However, the apparent stepwise loss of foram taxa may reflect the Signor-Lipps
285 Effect, in which incomplete preservation/identification of stratigraphic ranges obscures the signal of
286 a mass extinction event (Rampino and Adler, 1998). The comparatively poor preservation of

bioclasts at Lung Cam may have contributed to this effect.

The fossil assemblages of the study sections, which accumulated on different platforms in the Nanpanjiang Basin, thus provide evidence for a single abrupt extinction (i.e., the LPME) that was associated with the lithologic transition from Upper Permian bioclastic limestones to Lower Triassic microbialites. This extinction event led to the rapid disappearance of diverse fossil groups across the Nanpanjiang Basin, including all calcareous algae, sponges, brachiopods, as well as most foraminifers, e.g., *Nankinella* spp., *Reichelina* spp., *Palaeofusulina* spp., *Pachyphloia* spp. and *Robuloides* spp. This finding is consistent with results from other shallow platform successions in South China, Japan, and Europe (Payne et al., 2007; Wang et al., 2009; Song-HJ et al., 2009b, 2013).

A second extinction event of earliest Griesbachian (earliest Triassic) age, sometimes called the earliest Triassic mass extinction (ETME), corresponds to the contact of the *H. parvus* and *I. staeschei* Zones (Bed 28 at Meishan D; Song-HJ et al., 2013) and postdates the LPME by ~60 kyr (Burgess et al., 2014). This event records the loss of diverse fossil groups, including foraminifers, brachiopods, and conodonts (Jiang et al., 2007; Chen et al., 2009; Song-HJ et al., 2009a, 2013; He et al., 2015). This extinction event is distinct from the preceding LPME event, as both are clearly developed in multiple sections of the Yangtze Platform (e.g., Huangzhishan and Meishan D). This second extinction event is found within the *I. staeschei* conodont Zone at Meishan D, i.e., which is correlative with the demise of PTBM in the Nanpanjiang Basin (Chen et al., 2009; Song-HJ et al., 2013). However, the present study sections do not extend far enough into the Lower Triassic to record this second extinction event (Fig. 12).

Changes in benthic invertebrate community composition on carbonate platforms are often related to changes in water depths (Madi et al., 1996; Flügel, 2004). In this study, the abundances of

309 fusulinids increased from < 5 % in the lower part of each section (0–60 cm at Wengna; 0–620 cm at
310 Taiping) to > 40 % just below the LPME (60–75 cm at Wengna; 620–730 cm at Taiping) (Fig. 12).
311 Since fusulinids favored clear, shallow waters, and fusulinid-enriched biofacies have been observed
312 during Permian regressions (Dawson and Racey, 1993; Ross, 1995), we interpret the enrichment of
313 fusulinids in the uppermost Permian of these two study sections as an indicator of a shallowing trend
314 (Figs. 5 and 7). At Lung Cam, although vertical changes in fusulinid abundance are less clear, a
315 decrease in bivalves upsection combined with a microfacies shift from MF1 (molluscan packstone)
316 to MF2 (algal-foraminiferal packstone-grainstone) support the shallowing interpretation. Based on
317 the high-resolution zircon U-Pb timescale of Burgess et al. (2014), this interval represents ~20–30
318 kyr based on an average sedimentation rate of 2.6 cm/kyr) prior to the LPME (based on the thickness
319 and estimated average sedimentation rate in (Burgess et al., 2014).
320
321 *4.2. Spatial variation in fossil assemblages and oceanographic controls*
322 The Upper Permian bioclastic limestones of the present study sections contain much greater
323 abundances of fusulinids and algae (up to 50 %) than the correlative interval of the Meishan D
324 section (< 20 %). This difference is attributable to their paleogeographic locations. Meishan D was
325 located on the upper slope of a carbonate ramp (Fig. 1) that was subject to moderate terrigenous
326 detrital inputs (Tong and Yin, 2002; Algeo and Twitchett, 2010), and some combination of a
327 siliciclastic substrate and greater water-column turbidity suppressed growth of fusulinids and algae.
328 In contrast, the carbonate platforms of the Nanpanjiang Basin, on which the present study sections
329 are located (Fig. 1), were largely free of siliciclastic influence (Lehrmann et al., 2001, 2003, 2007;
330 Algeo and Twitchett, 2010). In addition, Meishan D contains relatively greater abundances of

bivalves and ostracods (> 20 %) than the present study sections (< 10 %) (Fig. 12). These taxa appear to have flourished more successfully than fusulinids and algae under conditions of elevated terrigenous detrital inputs, owing to their wide tolerances of variations in nutrient levels, substrate conditions, and watermass salinities (Attrill et al., 2000; Fraschetti et al., 2005; Dunlop et al., 2008).

Even within just the Nanpanjiang Basin, distinct spatial variations in fossil abundances are apparent among the three study sections: (1) bivalve fragments are rarely recorded at Wengna, comparing to their higher abundances at Taiping and Lung Cam; (2) ostracods are significantly enriched at Lung Cam; and (3) fusulinids are much more abundant in the uppermost Permian bioclastic limestone at Wengna and Taiping than at Lung Cam (Figs. 5, 7, 9 and 12). These differences are attributable to the locations of individual carbonate platforms in the Nanpanjiang Basin, with the Great Bank of Guizhou (Wengna section) being close to the Yangtze Platform, whereas the Pingguo and Jinxi Platforms (Taiping and Lung Cam sections, respectively) were located on the Panthalassic margin of the South China Craton (Fig. 1). Several factors may have influenced these patterns of spatial variation, especially (1) water depths, and (2) proximity to the open ocean. Fusulinids and algae show a strong preference for shallow waters (as at Wengna and Taiping), whereas bivalves and ostracods show preferences for deeper-water conditions (as at Lung Cam; n.b., a depth control on marine faunas was also documented by Song-HJ et al., 2013). Proximity to the open ocean influenced nutrient levels, with stronger upwelling of nutrients at Lung Cam leading to a higher density of grazers (e.g., ostracods and bivalves) and a smaller mass of algae. This pattern accords with observations of increased grazing pressure in modern eutrophic systems (Kotta et al., 2004).

353 *4.3. Pre-LPME "foram gap" and "detrital event"*

354 A "foram gap" was discovered at variable distances below the LPME in all three study sections:
355 40 cm at Wengna, 240 cm at Taiping, and 15 cm at Lung Cam below the formation contacts (Fig. 12).
356 Although all foram species disappeared completely within the foram gap, the majority of them
357 reappeared in the overlying strata. For example, 25 out of 30 taxa reappeared at Wengna, 17 out of
358 23 reappeared at Taiping (Fig. 7), and 11 out of 17 reappeared at Lung Cam (Fig. 9). In particular,
359 most of the wide-ranging Late Permian forms like *Nankinella* spp. and *Pachyphloia* spp. reappeared
360 following the foram gap, and the taxa that did not reappear were generally the ones that were less
361 common prior to the gap. The foram gap was associated with an influx of siliciclastics in the study
362 sections (see below), suggesting that the disappearance of forams was facies-related and possibly
363 triggered by a sudden surge of eroded material into shallow carbonate platform settings.

364 A transient facies change toward greater siliciclastic content (here termed the "detrital event") is
365 apparent in all three study sections at intervals of 15 cm to 2.4 m below the LPME horizon (Fig. 12),
366 in association with the foram gap. The sedimentary features associated with this facies change vary
367 somewhat from section to section. At Taiping, it is marked by a sandy limestone layer that contains
368 abundant quartz and feldspar grains (Fig. 11). The pre-LPME facies change at Lung Cam is similar
369 but with a higher proportion of micas (~15 %). The layer recording the pre-LPME facies change at
370 Wengna shows a sharp decline in bioclast content but does not exhibit visible detrital grains,
371 although an increase in Al_2O_3 (from 0.66 % to 2.68 %; Song-HY et al., 2014b) implies enhanced clay
372 content (Fig. 2). Thus, the pre-LPME facies change in all three study sections was associated with an
373 influx of detrital material.

374 Although the foram gap and detrital event are the same horizon in each of the three study

sections, the lack of sufficiently detailed biostratigraphic data precludes determination of whether these horizons are precisely synchronous among the study sections. One indication that they may be synchronous is that all three horizons are located in the same position within a C-isotope correlation framework, i.e., slightly above the level of the initial shift in the latest-Permian negative $\delta^{13}C$ excursion, which is equivalent to the upper Bed 23 and lower Bed 24 at Meishan (dotted line; Fig. 4). Burgess et al. (2014) estimated the age of this initial $\delta^{13}C$ decrease at Meishan as 251.999 ± 0.039 Ma, or ~60 kyr older than the LPME. In the context of this $\delta^{13}C$-based correlation scheme, the foram gap/detrital event horizons may be attributed to a regional (or global?) perturbation in the middle *Clarkina yini* Zone (Fig. 4). Numerous environmental and biotic anomalies had been reported in this interval, including photic-zone euxinia (Grice et al., 2005; Li et al., 2016), enhanced soil erosion (Kaiho et al., 2016; Zhou et al., 2016), elevated terrestrial inputs (Dudás et al., 2017), and declines in ammonoid size and morphological complexity (Kiessling et al., 2018).

The detrital event may reflect an increase in terrestrial erosion prior to the LPME, a hypothesis that is consistent with the larger and better-documented increase in erosion that accompanied the LPME. The increase in erosion at the LPME is recorded by enhanced soil erosion, higher marine shelf sedimentation rates, more radiogenic seawater Sr isotopes, and greater concentrations of clay minerals in marine sections (Retallack, 2005; Sheldon, 2006; Algeo et al., 2007, 2011; Algeo and Twitchett, 2010; Song-HJ et al., 2015). The trigger for erosion may have been acid rain and die-off of terrestrial vegetation as a consequence of the Siberian Traps eruptions (Newell et al., 1999; Ward et al., 2000; Algeo et al., 2011). The occurrences of siliciclastics in the uppermost Permian carbonates of our sections are unusual in that they occur before the LPME, but they may represent a precursor perturbation that resulted in a transient increase in detrital fluxes. Burgess and Bowring (2015)

provided evidence that an initial pulse of Siberian Traps magmatism triggered ecosystem perturbations up to 300 kyr prior to the LPME, whereas the LPME probably marks the main flood basalt eruption stage. The mechanism for transporting siliciclastics onto distal carbonate platforms in the Nanpanjiang Basin is not certain, but we hypothesize that large turbid plumes generated through massive soil erosion may have helped move siliciclastics offshore.

4.4. Faunal composition and environmental implications of PTBMs

Microbialites took the place of bioclastic limestones during the LPME, marking the most significant lithological and biotic transition on shallow carbonate platforms across South China (Figs. 2, 3) and in equivalent settings in Europe (Pruss et al., 2006; Baud et al., 2007; Xie et al., 2010; Yang et al., 2011; Kershaw et al., 2012a). The PTBMs were deposited on the underlying uppermost Permian bioclastic limestones along the "basal PTBM diastem" (Figs. 2, 3; also see Yang et al., 2011; Kershaw et al., 2012a). Yin et al. (2014) examined the biostratigraphic zonations of dozens of P-Tr boundary sections of different facies and concluded that part or all of the *Clarkina meishanensis* and *Hindeodus changxingensis* zones are commonly missing in shallow platform successions on the northern margin of the Yangtze Platform and on isolated platforms of the Nanpanjiang Basin. Where a hiatus is present in these shallow-marine sections, it is thought to represent an interval of 89 ± 38 kyr (as estimated by Baresel et al., 2017; it might be less in the present study sections based on the carbon isotope correlation in Section 4.3). Such a significant hiatus means that the details of biotic and environmental changes at the LPME (sensu stricto) cannot be reconstructed from shallow-carbonate successions in South China.

The growth morphology and abundance of marine invertebrate colonizers of the microbialites

may provide environmental insights during the latest Permian and earliest Triassic following the basal PTBM diastem. The PTBMs in the Nanpanjiang Basin are mostly thrombolitic, which contrasts with the stromatolitic growth form of Lower Triassic microbialites on the northern margin of the Yangtze Platform and at localities in the western Tethys (Kershaw et al., 2009, 2011; Adachi et al., 2017). In addition, the PTBMs in the Nanpanjiang Basin have a much greater metazoan fossil content than coeval stromatolitic mats, which tend to contain few marine invertebrates. These patterns have analogs on the modern Bahamian Platform, where thrombolites are characterized by a mixed bacterial-metaphyte ecosystem of greater complexity than the dominantly microbial biotas of stromatolitic mats (Planavsky and Ginsburg, 2009; Tarhan et al., 2013). Highly diverse metazoan assemblages are also present in thrombolites of Cambro-Ordovician age (Kennard and James, 1986) and in modern Lake Clifton, Western Australia (Moore and Burne, 1994; Konishi et al., 2001). These relationships may reflect variation in rates of microbial calcification versus metazoan bioerosion (Garcia-Pichel et al., 2004). The calcification rate is linked to the intensity of photosynthesis, which causes a local increase in watermass alkalinity, driving carbonate cement formation (Dupraz et al., 2009). On the other hand, metazoan grazing partially destroys biogenic carbonates, creating gaps in microbial structures that then are more likely to grow into thrombolites (Kennard and James, 1986). In this scenario, the balance of calcification to bioerosion is a function of light availability (mainly linked to water depth), nutrient input, and aqueous environmental conditions (e.g., temperature, salinity, and dissolved oxygen) that influence the abundance of metazoan grazers (cf. Moore and Burne, 1994).

The invertebrate faunal content of PTBMs has been examined in only a few studies (Payne et al., 2006; Yang et al., 2011; Forel et al., 2009, 2013; Tang et al., 2017). Here, we quantified the main

441 biotic components of the PTBM, including ostracods, gastropods, and two probable calcifying
442 cyanobacteria (described as coccoidal and *Renalcis*-like) (Figs. 5E, 7F, 11E, 11F). At Wengna and
443 Taiping, both coccoidal and *Renalcis*-like microbes were found in some samples although their
444 contents are very low (<2 % in most samples). These cyanobacteria are thought to have been the
445 primary builders of the microbialites (Lehrmann, 1999; Wang et al., 2005), but the quantified
446 contents are too low to support this scenario. Ostracods are relatively abundant (2–15 % in most
447 samples from Wengna and Taiping, ~20% in Lung Cam samples), and Forel et al. (2009, 2013)
448 proposed that they grazed on cyanobacteria in the PTBM. An additional faunal component of the
449 PTBM is the microconchids, which are present in moderate abundances (2–5 %) only at Wengna.
450 They have previously been reported from PTBMs at other locales, e.g., Cili and Dajiang (Yang et al.,
451 2011). Although the growth of PTBMs has been attributed to anoxic seafloor conditions during the
452 P-Tr transition, and marine hypoxia-anoxia in the aftermath of the LPME is well established
453 (Lehrmann, 1999; Algeo et al., 2007, 2008; Knoll et al., 2007; Bond and Wignall, 2010; Liao et al.,
454 2010, 2017; Wang et al., 2015; Elrick et al., 2017), the quantified skeletal composition of our study
455 sections does not support low-oxygen conditions as a major cause of PTBM growth. First, the
456 association of diverse metazoan groups in the PTBMs suggests generally well-oxygenated conditions
457 (Kershaw et al., 2009; Forel et al., 2009, 2013; Yang et al., 2011; Loope et al., 2013; Tang et al.,
458 2017). The present study demonstrates a similar relationship: bioclasts (mainly of gastropods and
459 ostracods) comprise 5–20 % of the PTBMs at Wengna and Taiping (Fig. 12). Second, redox
460 conditions in the Permian-Triassic ocean-surface layer could not have been anoxic except for very
461 brief intervals at most, because the ocean-surface layer would have been resupplied with oxygen
462 from the atmosphere quickly (at a scale of days to weeks; Broecker and Peng, 1974) if it ever went

463 anoxic. Brief episodes of anoxia might have developed as a consequence of upward chemocline
464 excursions (Kump et al., 2005), for which the Nhi Tao section in Vietnam has provided evidence in
465 the form of multiple, thin framboidal pyrite layers (Algeo et al., 2007, 2008). However, the
466 ocean-surface layer would have remained oxic probably >99% of the time despite expanded anoxia
467 at greater ocean depths (e.g., Feng and Algeo, 2014). Anoxia may have set the stage for a resurgence
468 of microbialites by decimating metazoans at the LPME, but it is unlikely to have been a factor in
469 sustaining microbial growth in the aftermath of the extinction event.
470
471 **5. Conclusions**
472 The foraminiferal distributions, skeletal variations and microfacies analyses documented in three
473 shallow carbonate platform successions (Wengna, Taiping, and Lung Cam) from the Nanpanjiang
474 Basin show common patterns during the P-Tr transition. All sections record (1) a transient influx of
475 detrital siliciclastics just prior to the LPME, accompanied by a foram gap; (2) a single foraminiferal
476 extinction event, at the level of the LPME, associated with a diastem; and (3) an abrupt replacement
477 of bioclast-rich Upper Permian limestones by lowermost Triassic thrombolitic microbialites
478 following the LPME. A general biotic decline and a shallowing trend in the pre-LPME Upper
479 Permian indicate that unstable marine environmental conditions developed prior to the mass
480 extinction event. The post-LPME transition to a thrombolitic microbialite facies containing an
481 abundant gastropod-ostracod biota was due mainly to decimation of Late Permian shallow-marine
482 biotas and not to persistent anoxia in these surface-ocean systems. Shallow carbonate platforms in
483 the Nanpanjiang Basin record a unique set of changes in lithologies, microfacies, and skeletal
484 compositions (i.e., different from those in deeper-water settings) that provide significant insights into

biotic and environmental responses to large-scale perturbations prior to and during the Permian-Triassic transition.

Acknowledgments

We thank Steve Kershaw and an anonymous reviewer for the review and constructive comments. This study was supported by the National Science Foundation of China (grants nos. 41530104, 41602024, 41302271 and 41661134047), the "111" project (B08030), the State Key Laboratory of Biogeology and Environmental Geology (GBL11605) and the Fundamental Research Funds for the Central University, University of Geosciences (Wuhan) (CUG 160842). This is part of a research project and international exchange programme to Li Tian (both funded by China Postdoctoral Science Foundation), and NERC grant NE/P013724/1 to Mike Benton for UK-China collaboration. It is also a contribution to IGCP 630.

References

Adachi, N., Asada, Y., Ezaki, Y., Liu, J., 2017. Stromatolites near the Permian-Triassic boundary in Chongyang, Hubei Province, South China: A geobiological window into palaeo-oceanic fluctuations following the end-Permian extinction. Palaeogeography, Palaeoclimatology, Palaeoecology 475, 55–69.

Algeo, T.J., Twitchett, R.J., 2010. Anomalous Early Triassic sediment fluxes due to elevated weathering rates and their biological consequences. Geology 38, 1023–1026.

Algeo, T.J., Ellwood, B., Nguyen, T.K.T., Rowe, H., Maynard, J.B., 2007. The Permian-Triassic boundary at Nhi Tao, Vietnam: Evidence for recurrent influx of sulfidic watermasses to a shallow-marine carbonate platform. Palaeogeography, Palaeoclimatology, Palaeoecology 252, 304–327.

Algeo, T., Shen, Y., Zhang, T., Lyons, T., Bates, S., Rowe, H., Nguyen, T.K.T., 2008. Association of ^{34}S-depleted pyrite layers with negative carbonate δ^{13}C excursions at the Permian-Triassic boundary: Evidence for upwelling of sulfidic deep-ocean water masses. Geochemistry, Geophysics, Geosystems 9(4), Q04025, doi: 10.1029/2007GC001823.

Algeo, T.J., Chen, Z.Q., Fraiser, M.L., Twitchett, R.J., 2011. Terrestrial-marine teleconnections in the collapse and rebuilding of Early Triassic marine ecosystems. Palaeogeography, Palaeoclimatology, Palaeoecology 308, 1–11.

514 Attrill, M.J., Strong, J.A., Rowden, A.A., 2000. Are macroinverbrate communities influenced by seagrass
515 structural complexity? Ecography 23, 114–121.

516 Bambach, R.K., 2002. Anatomical and ecological constraints on Phanerozoic animal diversity in the marine
517 realm. Proceedings of the National Academy of Sciences (U.S.A.) 99, 6854–6859.

518 Baresel, B., Bucher, H., Bagherpour B., Brosse, M., Guodun, K., Schaltegger, 2017. Timing of global
519 regression and microbial bloom linked with the Permian-Triassic boundary mass extinction: implications
520 for driving mechanisms. Scientific Reports 7, art. 43630.

521 Baud, A., Richoz, S., Marcoux, J., 2005. Calcimicrobial cap rocks from the basal Triassic units: western
522 Taurus occurrences (SW Turkey): Comptes Rendus Palevol 4, 569–582.

523 Baud, A., Richoz, S., Pruss, S., 2007. The lower Triassic anachronistic carbonate facies in space and time.
524 Global and Planetary Change 55, 81–89.

525 Bond, D.P.G., Wignall, P.B., 2010. Pyrite framboid study of marine Permian-Triassic boundary sections: a
526 complex anoxic event and its relationship to contemporaneous mass extinction. Geological Society of
527 America Bulletin 122 (7/8), 1265–1279.

528 Bottjer, D.J., Clapham, M.E., Fraiser, M.L., Powers, C.M., 2008. Understanding mechanisms for the
529 end-Permian mass extinction and the protracted Early Triassic aftermath and recovery. GSA Today 18,
530 4–10.

531 Brennecka, G.A., Herrmann, A.D., Algeo, T.J., Anbar, A.D., 2011. Rapid expansion of oceanic anoxia
532 immediately before the end-Permian mass extinction. Proceedings of the National Academy of
533 Sciences (U.S.A.) 108(43), 17631–17634.

534 Broecker, W.S., Peng, T.H., 1974. Gas exchange rates between air and sea. Tellus 26(1-2), 21–35.

535 Burgess, S.D., Bowring, S., Shen, S.Z., 2014. High-precision timeline for Earth's most severe extinction.
536 Proceedings of the National Academy of Sciences 11, 3316–3321.

537 Chen, Z.Q., Tong, J.N., Zhang, K.X., Yang, H., Liao, Z., Song, H.J., Chen, J., 2009. Environmental and biotic
538 turnover across the Permian–Triassic boundary on a shallow carbonate platform in western Zhejiang,
539 South China. Australian Journal of Earth Sciences 56(6), 775–797.

540 Chen, Z.Q., Yang, H., Luo, M., Benton, M.J., Kaiho, K., Zhao, L., Huang, Y., Zhang, K., Fang, Y., Jiang, H.,
541 2015. Complete biotic and sedimentary records of the Permian-Triassic transition from Meishan section,
542 South China: Ecologically assessing mass extinction and its aftermath. Earth-Science Reviews 149,
543 67–107.

544 Dawson, O., Racey, A., 1993. Fusuline-calcareous algal biofacies of the Permian Ratburi Limestone, Saraburi,
545 Central Thailand. Journal of Southeast Asian Earth Sciences 8, 49–65.

546 Dudás, F.Ö., Yuan, D.X., Shen, S.Z., Bowring, S.A., 2017. A conodont-based revision of the $^{87}Sr/^{86}Sr$ seawater
547 curve across the Permian-Triassic boundary. Palaeogeography, Palaeoclimatology, Palaeoecology 470,
548 40–53.

549 Dunlop, J.E., Horrigan, N., McgGreyor, G., Kelford, B.J., Choy, S., Prasad, R., 2008. Effect of spatial
550 variation on salinity tolerance of macroinvertebrates in Eastern Australia and implications for ecosystem
551 protection trigger values. Environmental Pollution 151, 621–630.

552 Dupraz, C., Reid, R.P., Braissant, O., Decho, A.W., Norman, R.S., Visscher, P.T., 2009. Processes of carbonate

553 precipitation in modern microbial mats. Earth-Science Reviews 96(3), 141–162.

554 Elrick, M., Polyak, V., Algeo, T.J., Romaniello, S., Asmerom, Y., Herrmann, A.D., Anbar, A.D., Zhao, L.,
555 Chen, Z.Q., 2017. Global-ocean redox variation during the middle-late Permian through Early Triassic
556 based on uranium isotope and Th/U trends of marine carbonates. Geology 45(2), 163–166.

557 Enos, P., Lehrmann, D.J., Wei J.Y., Yu, Y.Y., Xiao, J.F., Chaikin, D.H., Minzoni, M., Berry, A.K., Montgomery,
558 P., 2006. Triassic Evolution of the Yangtze Platform in Guizhou Province, People's Republic of China.
559 Geological Society of America Special Paper 417, 105 pp.

560 Ezaki, Y., Liu, J.B., Adachi, N., 2003. Earliest Triassic microbialite micro- to megastructures in the Huaying
561 area of Sichuan province, South China: Implications for the nature of oceanic conditions after the
562 end-Permian extinction. Palaios 18, 388–402.

563 Ezaki, Y., Liu, J.B., Nagano, T., Adachi, N., 2008. Geobiological aspects of the earliest Triassic microbialites
564 along the southern periphery of the tropical Yangtze Platform: Initiation and cessation of a microbial
565 regime. Palaios 23, 356–369.

566 Farabegoli, E., Perri, M., Posenato, R., 2007. Environmental and biotic changes across the Permian-Triassic
567 boundary in western Tethys: The Bulla parastratotype, Italy. Global and Planetary Change 55, 109–135.

568 Feng, Q., Algeo, T.J., 2014. Evolution of oceanic redox conditions during the Permo-Triassic transition:
569 Evidence from deepwater radiolarian facies. Earth-Science Reviews 137, 34–51.

570 Flügel, E., 2002. Triassic reef patterns. In: Kiessling, W., Flügel, E., Golonka, J. (Eds.), Phanerozoic Reef
571 Patterns, SEPM Special Publication 72, pp. 391–463.

572 Flügel, E., 2004. Microfacies of Carbonate Rocks: Analysis, Interpretation and Application. Springer-Verlag,
573 Berlin, 976 pp.

574 Forel, M.B., Crasquin, S., Kershaw, S., Feng, Q.L., Collin, P.Y., 2009. Ostracods (Crustacea) and water
575 oxygenation in the earliest Triassic of South China: implications for oceanic events at the end-Permian
576 mass extinction. Australian Journal of Earth Sciences 56, 815–823.

577 Forel, M.B., Crasquin, S., Kershaw, S., Collin, P.Y., 2013. In the aftermath of the end-Permian extinction: the
578 microbialite refuge? Terra Nova 25, 137–143.

579 Fraschetti, S., Terlizzi, A., Benedetti-Cecchi, L., 2005. Patterns of distribution of marine assemblages from
580 rocky shores: evidenc of relevant scales of variation. Marine Ecology Process Series 296, 13–29.

581 Garcia-Pichel, F., Al-Horani F.A., Farmer, J.D., Ludwig, R., Wade, B.D., 2004. Balance between microbial
582 calcification and metazoan bioerosion in modern stromatolitic oncolites. Geobiology 2, 49–57.

583 Gorjan, P., Kaiho, K., Kakegawa, T., Niitsuma, S., Chen, Z.Q., Kaiiwara, Y., Nicora, A., 2007. Paleoredox,
584 biotic and sulfur-isotopic changes associated with the end-Permian mass extinction in the western Tethys.
585 Chemical Geology 244, 483–492.

586 Grice, K., Cao, C., Love, G.D., Böttcher, M.E., Twitchett, R.J., Grosjean, E., Summons, R.E., Turgeon, S.C.,
587 Dunning, W., Jin, Y., 2005. Photic zone euxinia during the Permian–Triassic superanoxic event. Science
588 307, 706–709.

589 He, W.H., Shi, G.R., Twitchett, R.J., Zhang, Y., Zhang, K.X., Song, H.J., Yue, M.L., Wu, S.B., Wu, H.T., Yang,
590 T.L., Xiao, Y.F., 2015. Late Permian marine ecosystem collapse began in deeper waters: evidence from
591 brachiopod diversity and body size changes. Geobiology 13, 123–138.

592 Jiang, H.S., Lai, X.L., Luo, G.M., Aldridge, R.J., Zhang, K.X., Wignall, P.B., 2007. Restudy of conodont
593 zonation and evolution across the P/T boundary at Meishan section, Changxing, Zhejiang, China. Global
594 and Planetary Change 55, 39–55.

595 Jiang, H.S., Lai, X., Sun, Y., Wignall, P.B., Liu, J., Yan, C., 2014. Permian-Triassic conodonts from Dajiang
596 (Guizhou, South China) and their implication for the age of microbialite deposition in the aftermath of
597 the End-Permian mass extinction. Journal of Earth Science [China University of Geosciences-Wuhan] 25,
598 413–430.

599 Kaiho, K., Chen, Z.Q., Kawahata, H., Kajiwara, Y., Sato, H., 2006. Close-up of the end-Permian mass
600 extinction horizon recorded in the Meishan section, South China: sedimentary, elemental, and biotic
601 characterization and a negative shift of sulfate sulfur isotope ratio. Palaeogeography, Palaeoclimatology,
602 Palaeoecology 239, 396–405.

603 Kaiho, K., Saito, R., Ito, K., Miyaji, T., Biswas, R., Li, T., Sano, H., Shi, Z., Takahashi, S., Tong, J., 2016.
604 Effects of soil erosion and anoxic-euxinic ocean in the Permian-Triassic marine crisis. Heliyon 2, e00137.

605 Kennard, J.M., James, N.P., 1986. Thrombolites and stromatolites: two distinct types of microbial
606 structures. Palaios 1, 492–503.

607 Kershaw, S., Li, Y., Crasquin-Soleau, S., Feng, Q., Mu, X., Collin, P.-Y., Reynolds, A., Guo, L., 2007. Earliest
608 Triassic microbialites in the South China block and other areas: controls on their growth and distribution.
609 Facies 53, 409–425.

610 Kershaw, S., Crasquin, S., Collin, P.-Y., Li, Y., Feng, Q., Forel, M., 2009. Microbialites as disaster forms in
611 anachronistic facies following the end-Permian mass extinction: a discussion. Australian Journal of Earth
612 Sciences 56, 809–813.

613 Kershaw, S., Crasquin, S., Li, Y., Collin, P.Y., Forel, M.B., Mu, X., Baud, A., Wang, Y., Xie, S., Maurer, F.,
614 2012a. Microbialites and global environmental change across the Permian-Triassic boundary: a synthesis.
615 Geobiology 10, 25–47.

616 Kershaw, S., Crasquin, S., Li, Y., Collin, P.-Y., Forel, M.-B., 2012b. Ocean acidification and the end-Permian
617 mass extinction: To what extent does evidence support hypothesis? Geosciences 2(4), 221–234.

618 Kiessling, W., Schobben, M., Ghaderi, A., Hairapetian, V., Leda, L., Korn D., 2018. Pre-mass extinction
619 decline of latest Permian ammonoids. Geology 46(3), 283–286.

620 Knoll, A.H., Fischer, W.W., 2011. Skeletons and ocean chemistry: The long view. In: Gattuso, J.P., Hansson, L.
621 (Eds.), Ocean Acidification, Oxford University Press, New York, pp. 67–82.

622 Knoll, A.H., Bambach, R.K., Canfield, D.E., Grotzinger, J.P., 1996. Comparative Earth history and Late
623 Permian mass extinction. Science 273, 452–457.

624 Knoll, A.H., Bambach, R.K., Payne, J.L., Pruss, S., Fischer, W.W., 2007. Paleophysiology and end-Permian
625 mass extinction. Earth and Planetary Science Letters 256, 295–313.

626 Konishi, Y., Prince, J., Knott, B., 2001. The fauna of thrombolitic microbialites, Lake Clifton, Western
627 Australia. Hydrobiologia 45, 39–47.

628 Kotta, J., Torn, K., Martin, G., Orav-Kotta, H., Paalmc, T., 2004. Seaonal variation in invertebrate grazing on
629 *Chara connivens* and *C. tomentosa* in Koiguste Bay, NE Baltic Sea. Helgoland Marine Research 58,
630 71–76.

631 Kump, L.R., Pavlov, A., Arthur, M.A., 2005. Massive release of hydrogen sulfide to the surface ocean and
632 atmosphere during intervals of oceanic anoxia. Geology 33(5), 397–400.

633 Lehrmann, D.J., 1999. Early Triassic calcimicrobial mounds and biostromes of the Nanpanjiang basin, south
634 China. Geology 27, 359–362.

635 Lehrmann, D.J., Wei, J., Enos, P., 1998. Controls on facies architecture of a large Triassic carbonate platform:
636 the Great Bank of Guizhou, Nanpanjiang Basin, South China. Journal of Sedimentary Research 68(2),
637 311–326.

638 Lehrmann, D.J., Wan, Y., Wei, J., Yu, Y., Xiao, J., 2001. Lower Triassic peritidal cyclic limestone: an example
639 of anachronistic carbonate facies from the Great Bank of Guizhou, Nanpanjiang Basin, Guizhou Province,
640 South China. Palaeogeography, Palaeoclimatology, Palaeoecology 173, 103–123.

641 Lehrmann, D.J., Payne, J.L., Felix, S.V., Dillett, P.M., Wang, H.M., Yu, Y.Y., Wei, J.Y., 2003. Permian-Triassic
642 boundary sections from shallow-marine carbonate platforms of the Nanpanjiang Basin, South China:
643 implications for oceanic conditions associated with the end-Permian extinction and its aftermath. Palaios
644 18, 138–152.

645 Lehrmann, D.J., Payne, J.L., Pei, D., Enos, P., 2007. Record of the end-Permian extinction and Triassic
646 recovery in the Chongzuo-Pingguo platform southern Nanpanjiang basin, Guangxi, south China.
647 Palaeogeography, Palaeoclimatology, Palaeoecology 252, 200–217.

648 Li, F., Yan, J., Chen, Z.Q., Ogg, J., Tian, L., Korngreem, D., Liu, K., Ma, Z.l., Woods, A., 2015. Global oolite
649 deposits across the Permian-Triassic boundary: A synthesis and implications for palaeoceanography
650 immediately after the end-Permian biocrisis. Earth-Science Reviews 149, 163–180.

651 Li, G.S. Wang, Y.B., Shi, G.R., Liao, W., Yu, L.X., 2016. Fluctuations of redox conditions across the
652 Permian-Triassic boundary—New evidence from the GSSP section in Meishan of South China.
653 Palaeogeography, Palaeoclimatology, Palaeoecology 448, 48–58.

654 Liao, W., Wang, Y.B., Kershaw, S., Weng, Z.T., Yang, H., 2010. Shallow-marine dysoxia across the
655 Permian-Triassic boundary: Evidence from pyrite framboids in the microbialite in South China.
656 Sedimentary Geology 232, 77–83.

657 Liao, W., Bond, D.P.G., Wang, Y.B., He, L., Yang, H., Weng, Z.T., Li, G.S., 2017. An extensive anoxic event in
658 the Triassic of the South China Block: A pyrite framboid study from Dajiang and its implications for the
659 causes of oxygen depletion. Palaeogeography, Palaeoclimatology, Palaeoecology 486, 86–95.

660 Luo, G.M., Wang, Y., Yang, H., Algeo, T.J., Kump, L.R., Huang, J., Xie, S., 2011. Stepwise and
661 large-magnitude negative shift in $\delta^{13}C_{carb}$ preceded the main marine mass extinction of the
662 Permian-Triassic crisis interval. Palaeogeography, Palaeoclimatology, Palaeoecology 299, 70–82.

663 Madi, A., Bourque, P.A., Mamet, B.L., 1996. Depth-related ecological zonation of a Carboniferous carbonate
664 ramp: Upper Viséan of Béchar Basin, Western Algeria. Facies 35(1), 59–79.

665 Moore, L.S., Burne, R.V., 1994. The modern thrombolites of Lake Clifton, western Australia.
666 In: Bertrand-Sarfati, J., Monty, C. (Eds.), Phanerozoic Stromatolites II, Springer Netherlands, pp. 3–29.

667 Newell, A.J., Tverdokhlebov, V.P., Benton, M.J., 1999. Interplay of tectonics and climate on a transverse
668 fluvial system, Upper Permian, Southern Uralian Foreland Basin, Russia. Sedimentary Geology 127,
669 11–29.

Payne, J.L., Clapham, M.E., 2012. End-Permian mass extinction in the oceans: an ancient analog for the twenty-first century? Annual Review of Earth and Planetary Sciences 40, 89–111.

Payne, J.L., Lehrmann, D.J., Wei, J., Orchard, M.J., Schrag, D.P., Knoll, A.H., 2004. Large perturbations of the carbon cycle during recovery from the end-Permian extinction. Science 305, 506–509.

Payne, J.L., Lehrmann, D.J., Wei, J., Knoll, A.H., 2006. The pattern and timing of biotic recovery from the end-Permian extinction on the Great Bank of Guizhou, Guizhou Province, China. Palaios 21, 63–85.

Payne, J.L., Lehrmann, D., Follett, D., Seibel, M., Kump, L.P., Riccardi, A., Altiner, D., Sano, H., Wei, J., 2007. Erosional truncation of uppermost Permian shallow-marine carbonates and implications for Permian-Triassic boundary events. Geological Society of America Bulletin 119, 771–784.

Planavasky, N., Ginsburg, R., 2009. Taphonomy of modern Bahamian microbialites. Palaios 24(1), 5–17.

Pruss, S.B., Bottjer, D.J., Corsetti, F.A., Baud, A., 2006. A global marine sedimentary response to the end-Permian mass extinction: Examples from southern Turkey and the western United States. Earth-Science Reviews 78, 193–206.

Rampino, M.R., Adler, A.C., 1998. Evidence for abrupt latest Permian mass extinction of foraminifera: Results of tests for the Signor-Lipps effect. Geology 26(5), 415–418.

Raup, D.M., 1979. Size of the Permo-Triassic bottleneck and its evolutionary implications. Science 206(4415), 217–218.

Retallack, G.J., 2005. Earliest Triassic claystone breccias and soil-erosion crisis. Journal of Sedimentary Research 75(4), 679–695.

Ross, C.A., 1995, Permian fusulinaceans. In: Scholle, P.A., Peryt, T.M., Ulmer-Scholle, D.S. (eds.), The Permian of Northern Pangea: Berlin, Springer-Verlag, pp. 167–185.

Sheldon, N.D., 2006. Abrupt chemical weathering increase across the Permian–Triassic boundary. Palaeogeography, Palaeoclimatology, Palaeoecology 231(3-4), 315–321.

Shen, S., Crowley, J.L., Wang, Y., Bowring, S.A., Erwin, D.H., Sadler, P.M., Cao, C., Rothman, D.H., Henderson, C.M., Ramezani, J., 2011. Calibrating the end-Permian mass extinction. Science 334, 1367–1372.

Son, T.H., Koeberl, C., Ngoc, N.L., Huyen, D.T., 2007. The Permian-Triassic boundary sections in northern Vietnam (Nhi Tao and Lung Cam sections): Carbon-isotope excursion and elemental variations indicate major anoxic event. Palaeoworld 16, 51–66.

Song, H.J., Tong, J., Chen, Z.Q., 2009a. Two episodes of foraminiferal extinction near the Permian-Triassic boundary at the Meishan section, South China. Australian Journal of Earth Sciences 56, 765–773.

Song, H.J., Tong, J., Chen, Z.Q., Yang, H., Wang, Y., 2009b. End-Permian mass extinction of foraminifers in the Nanpanjiang Basin, South China. Journal of Paleontology 83(5), 718–738.

Song, H.J., Wignall, P.B., Tong, J., Yin, H., 2013. Two pulses of extinction during the Permian-Triassic crisis. Nature Geoscience 6, 52–56.

Song, H.J., Wignall, P.B., Chu, D., Tong, J., Sun, Y., Song, H.Y., He, W., Tian, L., 2014. Anoxia/high temperature double whammy during the Permian-Triassic marine crisis and its aftermath. Scientific Reports 4, 4132.

Song, H.J., Wignall, P.B., Tong, J.N., Song, H.Y., Chen, J., Chu, D.L., Tian, L., Luo, M., Zong, K.Q., Chen, Y.L., Lai, X.L., Zhang, K.X., Wang, H.M., 2015. Integrated Sr isotope variations and global environmental changes through the Late Permian to early Late Triassic. Earth and Planetary Science Letters 424, 140–147.

Song, H.Y., Tong, J., Algeo, T.J., Song, H.J., Qiu, H., Zhu, Y., Tian, L., Bates, S., Lyons, T.W., Luo, G., Kump, L.R., 2014a. Early Triassic seawater sulfate drawdown. Geochimica et Cosmochimica Acta 128, 95–113.

Song, H.Y., Tong, J.N., Tian, L., Song, H.J., Qiu, H.O., Zhu, Y.Y., Algeo, T., 2014b. Paleo-redox conditions across the Permian-Triassic boundary in shallow carbonate platform of the Nanpanjiang Basin, South China. Science in China D: Earth Science 57, 1030–1038.

Tang, H., Kershaw, S., Liu, H., Tan, X.C., Li, F., Hu, G., Huang, C., Wang, L.C., Lian, C.B., Li, L., Yang, X.F., 2017. Permian-Triassic boundary microbialites (PTBMs) in southwest China: implications for paleoenvironment reconstruction. Facies 63(1), art. 2, 23 pp.

Tarhan, I.G., Planavsky, N.J., Laumer, C.E., Stolz, J.E., Reid, R.P., 2013. Microbial mat controls on infaunal abundance and diversity in modern marine microbialites. Geobiology 11, 485–497.

Tian, L., Tong, J.N., Sun, D., Xiong, Y., Wang, C., Song, H.J., Song, H.Y., Huang, Y., 2014a. The microfacies and sedimentary responses to the mass extinction during the Permian-Triassic transition at Yangou Section, Jiangxi Province, South China. Science in China D: Earth Sciences 57, 2195–2207.

Tian, L., Tong, J.N., Algeo, T.J., Song, H.J., Chu, D.L., Shi, L., Bottjer, D.J., 2014b. Reconstruction of Early Triassic ocean redox conditions based on framboidal pyrites from the Nanpanjiang Basin, South China: Palaeogeography, Palaeoclimatology, Palaeoecology 412, 68–79.

Tian, L., Tong, J.N., Bottjer, D., Chu, D., Liang, L., Song, H.J., Song, H.Y., 2015a. Rapid carbonate depositional changes following the Permian-Triassic mass extinction: Sedimentary evidence from South China. Journal of Earth Science [China University of Geosciences-Wuhan] 26, 166–180.

Tian, L., Bottjer, D.J., Tong, J.N., Fei, L., Yang, T.L., Song, H.J., Song, H.Y., Liang, L., 2015b. Distribution and size variation of ooids in the aftermath of the Permian-Triassic mass extinction. Palaios 30, 714–727.

Tong, J., Yin, H., 2002. The Lower Triassic of South China. Journal of Asian Earth Sciences 20(7), 803–815.

Wang, L., Wignall, P.B., Wang, Y., Jiang, H., Sun, Y., Li, G., Yuan, J., Lai, X., 2015. Depositional conditions and revised age of the Permo-Triassic microbialites at Gaohua section, Cili County (Hunan Province, South China). Palaeogeography, Palaeoclimatology, Palaeoecology 443, 156–166.

Wang, Q., Tong, J.N., Song, H.J., Yang, H., 2009. Ecological evolution across the Permian/Triassic boundary at the Kangjiaping Section in Cili County, Hunan Province, China. Science in China D: Earth Sciences 52, 797–806.

Wang, Y., Tong, J., Wang, J., Zhou, X., 2005. Calcimicrobialite after end-Permian mass extinction in South China and its palaeoenvironmental significance. Chinese Science Bulletin 50, 665–671.

Ward, P.D., Montgomery, D.R., Smith, R., 2000. Altered river morphology in South Africa related to the Permian-Triassic extinction. Science 289, 1740–1743.

Weidlich, O., Kiessling, W., Flügel, E., 2003. Permian-Triassic boundary interval as a model for forcing marine ecosystem collapse by long-term atmospheric oxygen drop. Geology 31, 961–964.

Woods, A.D., 2014. Assessing Early Triassic paleoceanographic conditions via unusual sedimentary fabrics

and features. Earth-Science Reviews 137, 6–18.

Xie, S., Pancost, R.D., Huang, J., Wignall, P.B., Yu, J., Tang, X., Chen, L., Huang, X., Lai, X., 2007. Changes in the global carbon cycle occurred as two episodes during the Permian-Triassic crisis. Geology 35, 1083–1086.

Xie, S., Pancost, R.D., Wang, Y., Yang, H., Wignall, P.B., Luo, G., Jia, C., Chen, L., 2010. Cyanobacterial blooms tied to volcanism during the 5 my Permo-Triassic biotic crisis. Geology 38, 447–450.

Yang, H., Chen, Z., Wang, Y., Tong, J., Song, H.J., Chen, J., 2011. Composition and structure of microbialite ecosystems following the end-Permian mass extinction in South China. Palaeogeography, Palaeoclimatology, Palaeoecology 308, 111–128.

Yin, H., Jiang, H., Xia, W., Feng, Q., Zhang, N., Shen, J., 2014. The end-Permian regression in South China and its implication on mass extinction. Earth-Science Reviews 137, 19–33.

Zhang, F.F., Romaniello, S.J., Algeo, T.J., Lau, K.V., Clapham, M.E., Richoz, S., Herrmann, A.D., Smith, H., and Anbar, A.D., 2018. Multiple episodes of extensive oceanic anoxia linked to global warming and continental weathering following the latest Permian mass extinction. Science Advances 4(4), e1602921.

Zhou, W., Algeo, T.J., Ruan, X., Luo, G., Chen, Z.Q., Xie, S., 2017. Expansion of photic-zone euxinia during the Permian-Triassic biotic crisis and its causes: Microbial biomarker records. Palaeogeography Palaeoclimatology Palaeoecology 474, 140–151.

Figures and captions

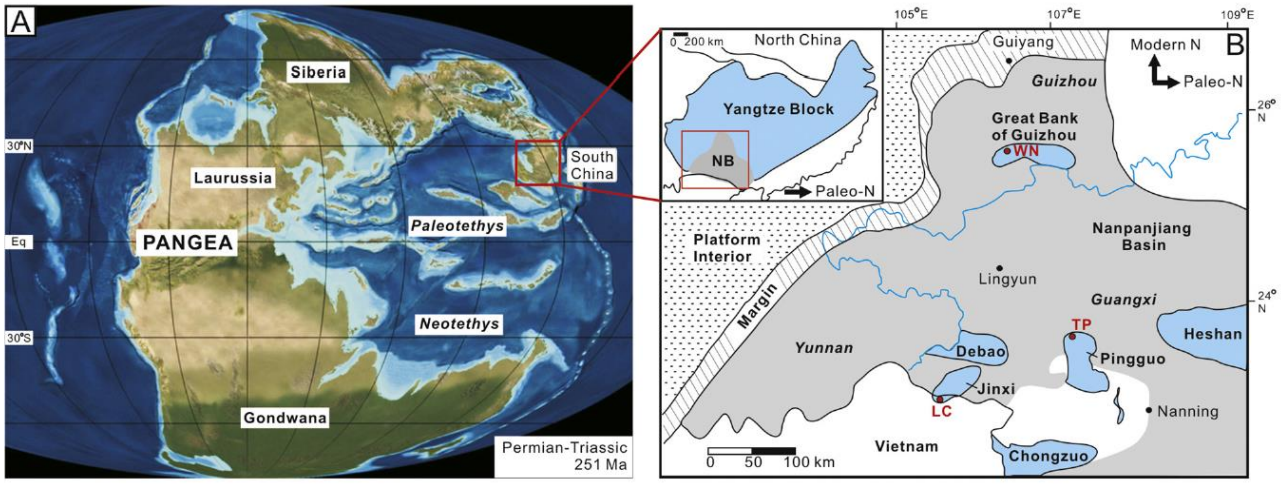

Fig. 1. Paleogeography of (A) the world and (B) the Nanpanjiang Basin of the South China Craton during the P-Tr transition. Map B shows the study section locations (red) on isolated carbonate platforms (blue): WN = Wengna, TP = Taiping, LC = Lung Cam. Map A is adapted from Ron Blakey (http://jan.ucc.nau.edu/rcb7/) and map B from Lehrmann et al. (2003) and Algeo et al. (2007). Note

772 that the South China Craton has rotated ~80° clockwise since the Permian-Triassic.

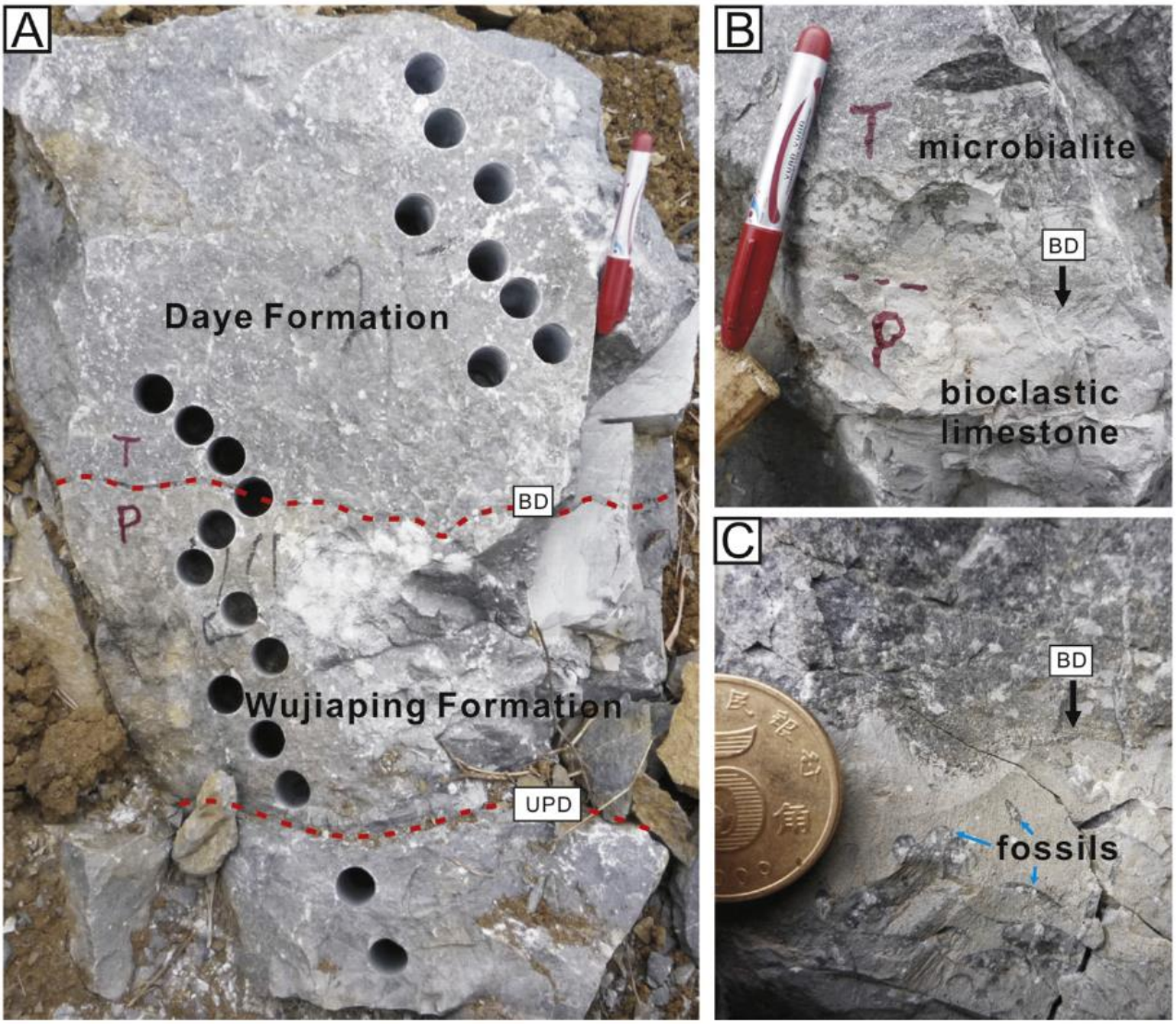

773

774 **Fig. 2.** Outcrop photos of the Wengna section. (A) Sampling of the P-Tr boundary interval using a
775 portable core drill. (B) Uppermost Permian bioclastic limestone overlain by lowermost Triassic
776 microbialite. (C) Close-up view of the contact between Permian bioclastic limestones and overlying
777 Triassic microbialites. The dotted lines in (A) indicate two distinct diastem surfaces: BD = basal
778 PTBM diastem; UPD = uppermost Permian diastem. Note diameter of the coin is 2 cm.

Fig. 3. Outcrop of the Taiping road section. (A) Uppermost Heshan and lowermost Majiaoling formations (the PTB is at the formation contact; red line). (B) Contact between uppermost Permian bioclastic limestones and lowermost Triassic microbialites. The lowermost Triassic diastem (LTD) is a stylolitized surface (blue arrow); BD = basal PTBM diastem (red arrow); BL = bioclastic limestone. (C) Thrombolites within Triassic microbialite interval, MF = micritic framework; SC = sparry cement (ruler = 10 cm).

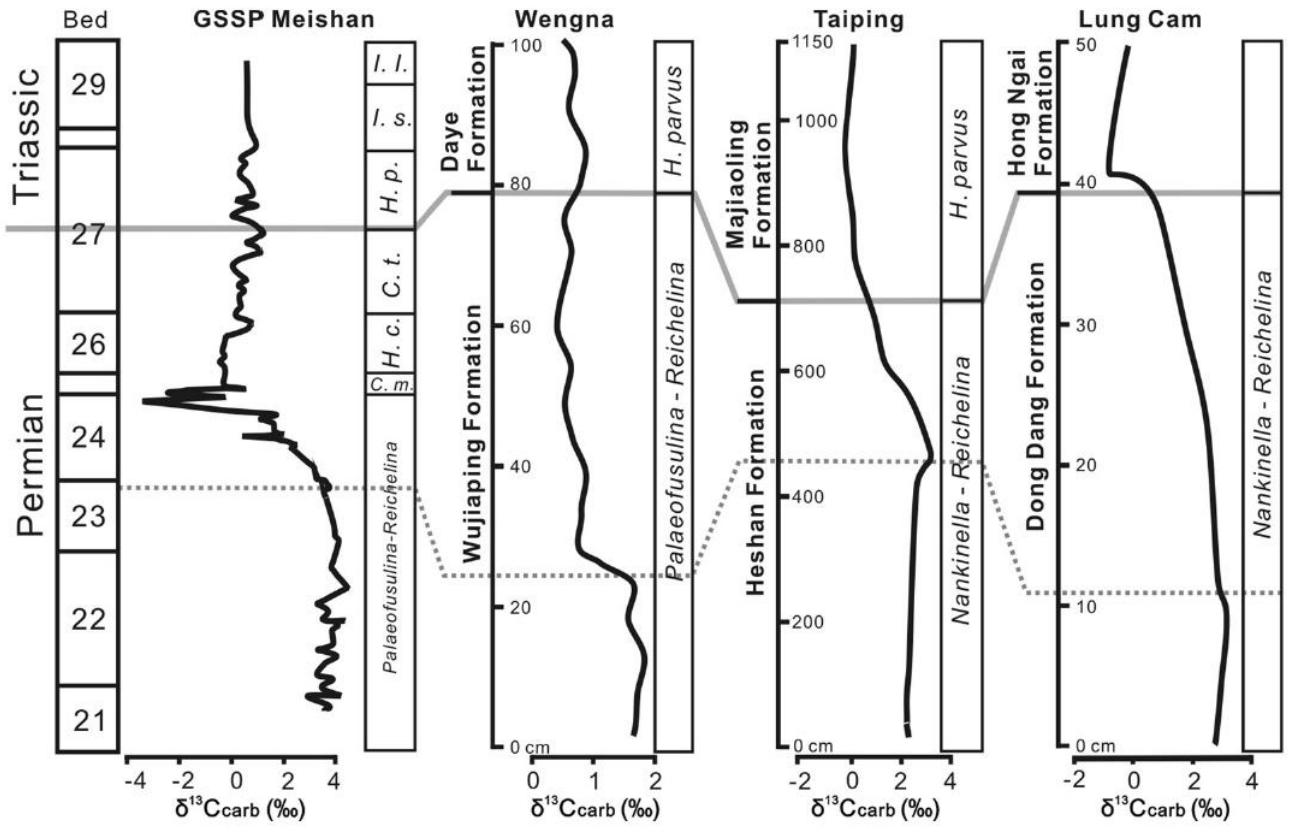

786

787 **Fig. 4.** Carbon-isotope correlation of study sections with the Meishan GSSP. The solid grey line
788 show PTB while the grey dashed line show initial negative shift of C-isotope. *C. m. = Clarkina*
789 *meishanensis*, *H. c. = Hindeodus changxingensis*, *C. t. = Clarkina taylorae*, *H. p. = Hindeodus*
790 *parvus*, *I. s. = Isarcicella staeschei*. For Meishan, conodont data are from Jiang et al. (2007),
791 foraminiferal data are from Song-HJ et al. (2009a) and C-isotope data from Shen et al. (2011).
792 C-isotope data for Wengna, Taiping, and Lung Cam are from Song-HY et al. (2014b), Luo et al.
793 (2011), and Son et al. (2007), respectively, while the foraminiferal data of these sections are from this
794 study. Conodont data for Wengna and Taiping are from Jiang et al. (2014) and unpublished conodont
795 study.

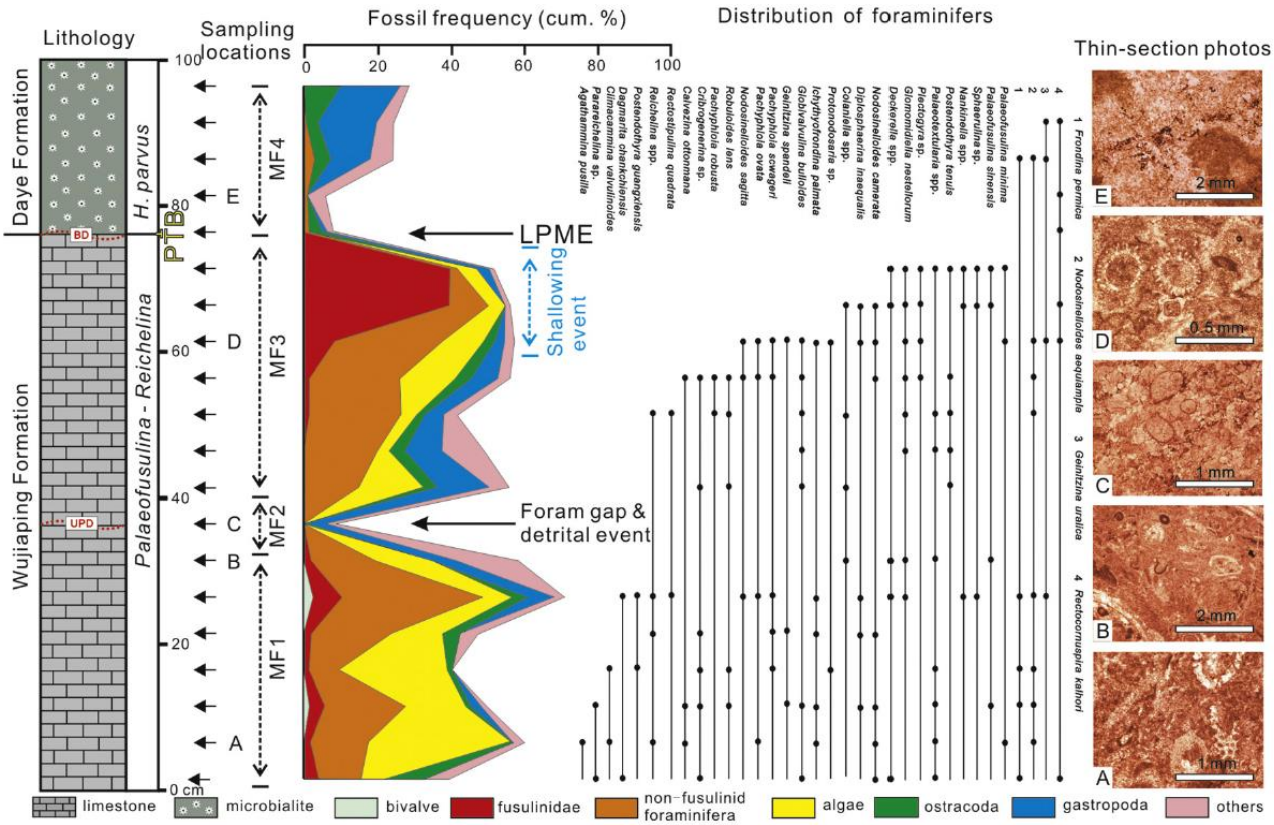

Fig. 5. Skeletal composition and foraminiferal distribution in the Wengna section. MF1: algal-foraminiferal packstone-grainstone; MF2: dolomitized wackestone; MF3: algal-foraminiferal grainstone; MF4: dolomitized gastropod wackestone. Fossil frequency = fossil count / total count × 100 % (based on point-counting in thin sections). BD = basal PTBM diastem; UPD = uppermost Permian diastem.

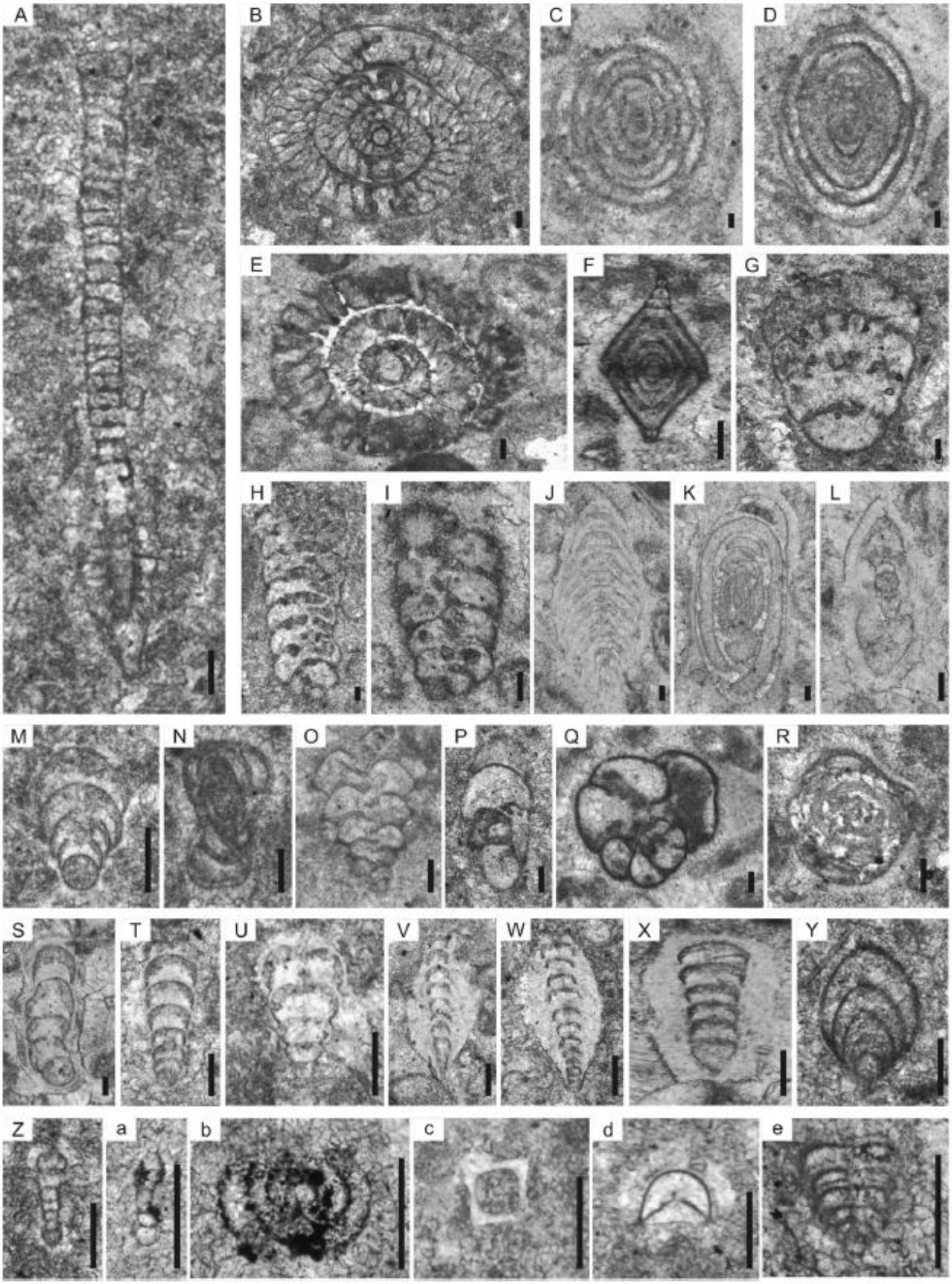

802

803 **Fig. 6.** Foraminifers from the Wengna section. (A) *Parareichelina* sp., WN0104 (specimen number);

(B) *Palaeofusulina sinensis*, WN0327; (C–D) *Nankinella* sp., C, WN1404, D, WN021505; (E) *Palaeofusulina sinensis*, WN1515; (F) *Reichelina* sp., WN0205; (G) *Cribrogenerina* sp., WN0408; (H) *Climacammina valvulinoides*, WN0407; (I) *Palaeotextularia* sp., WN1021; (J) *Colaniella* sp., WN1127; (K) *Agathammina pusilla*, WN0708; (L) *Robuloides lens*, WN0901; (M) *Frondina permica*, WN0110; (N) *Neodiscus plectogyraeformis*, WN1517; (O) *Dagmarita chanakchiensis*, WN0639; (P) *Postendothyra guangxiensis*, WN0405; (Q) *Postendothyra* sp., WN1103; (R) *Glomomidiella nestellorum*, WN1513; (S) *Calvezina ottonmana*, WN1214; (T) *Nodosinelloides tenuiseptata*, WN1354; (U) *Nodosinelloides camerata*, WN1335; (V–W) *Pachyphloia ovata*, V, WN1375, W, WN0401; (X) *Pachyphloia robusta*, WN1125; (Y) *Ichthyofrondina palmata*, WN0331; (Z) *Protonodosaria* sp., WN0406; (a–b) *Rectocorunspira kalhori*, a, WN1611, b, WN1709; (c) *Rectostipulina quadrata*, WN0603; (d) *Diplosphaerina inaequalis*, WN0631; and (e) *Geinitzina uralica*, WN1902. All scale bars are 0.1 mm in length.

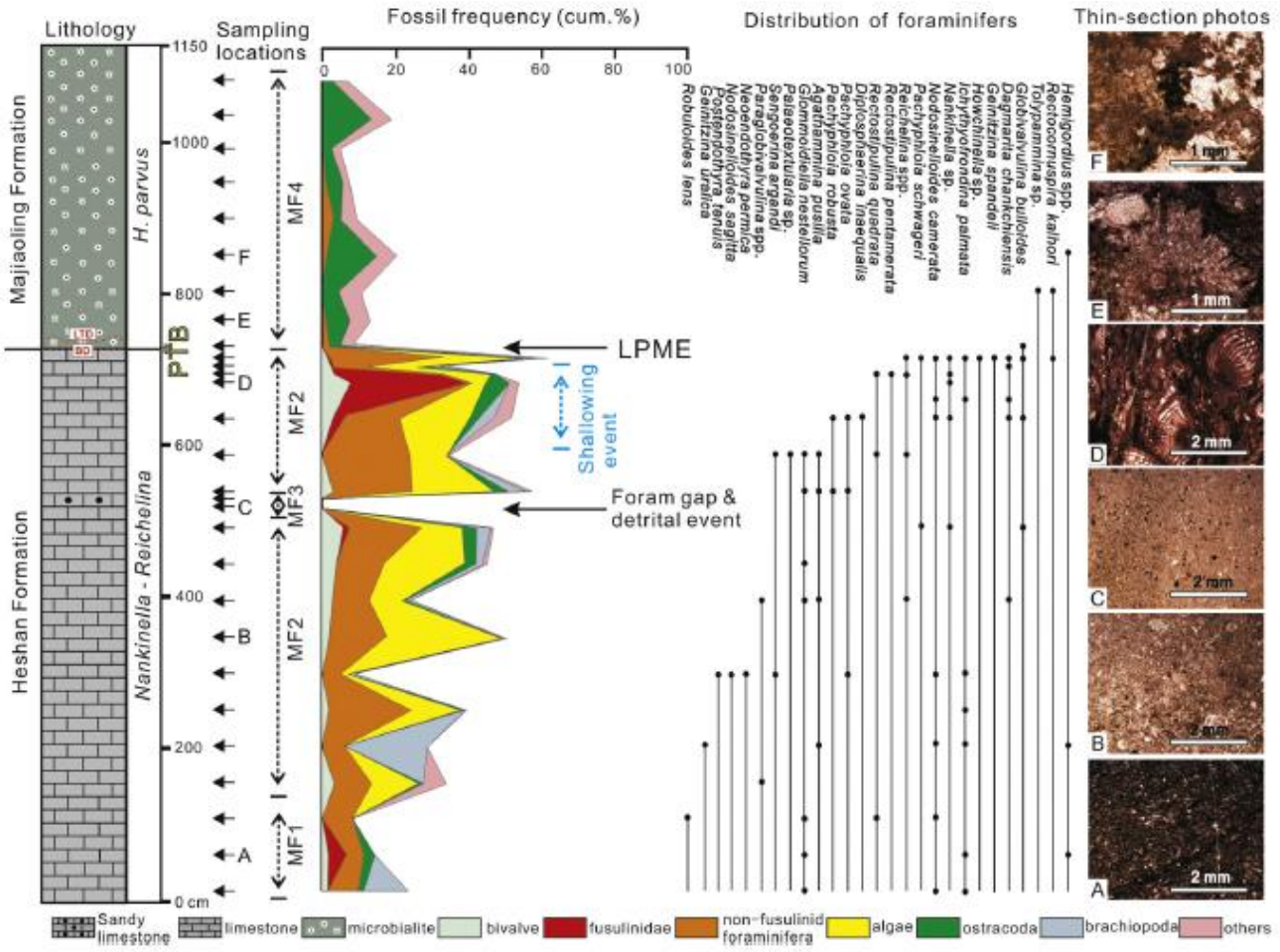

816

817 **Fig. 7.** Skeletal composition and foraminiferal distribution in the Taiping section. MF1: foraminiferal
818 packstone; MF2: algal-foraminiferal packstone; MF3: sandy mudstone; MF4: dolomitized
819 wackestone. Fossil frequency = fossil count / total count × 100 % (based on point-counting in thin
820 sections). BD = basal PTBM diastem; LTD = lowermost Triassic diastem.

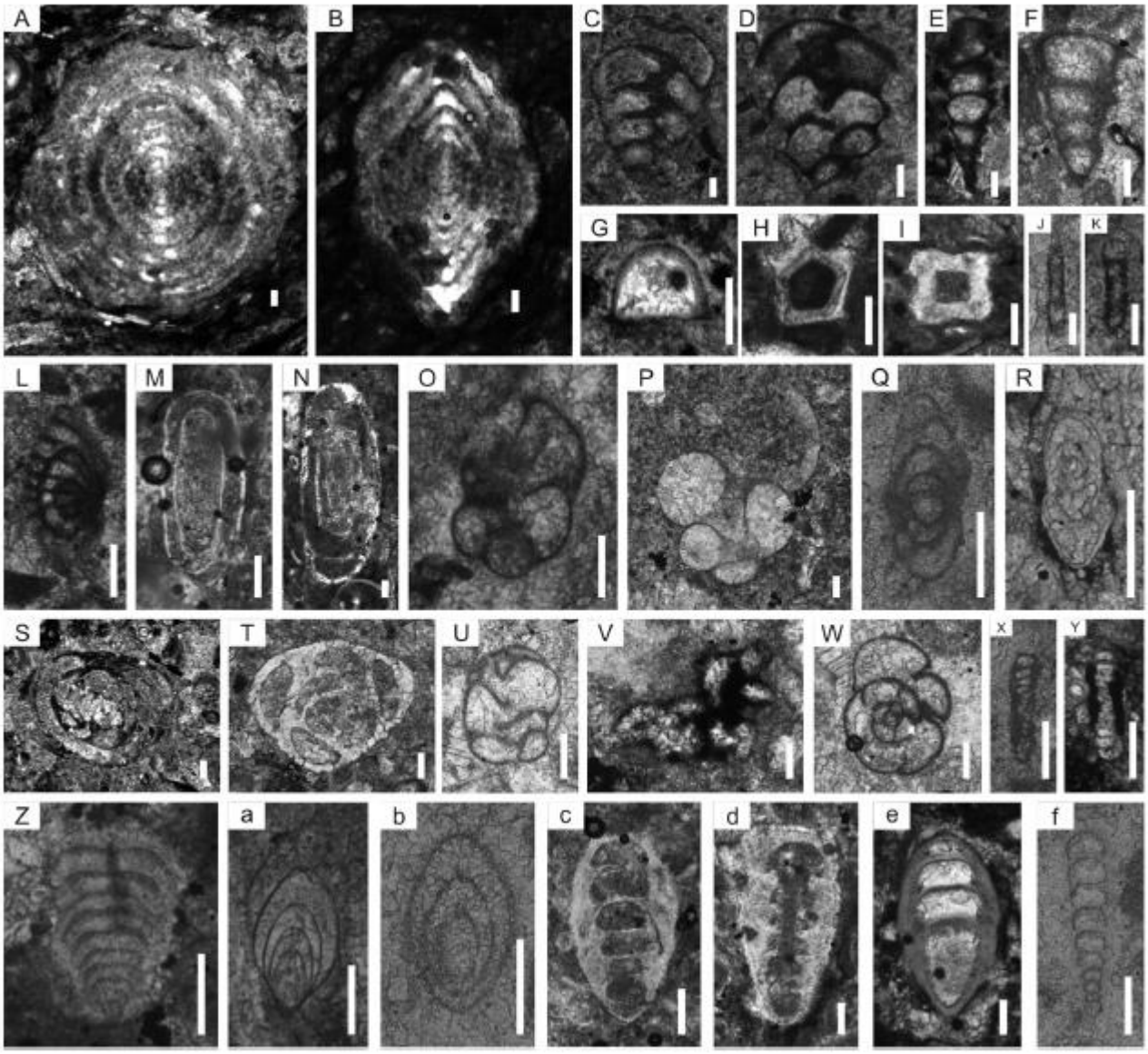

Fig. 8. Foraminifers from the Taiping section. (A–B) *Nankinella* sp., A, TP-2004 (specimen number), B, TP+2102; (C) *Palaeotextularia* sp., TP+0511; (D–F) *Dagmarita chanakchiensis*, D, TP+0507, E, TP+1004, F，TP+2404; (G) *Diplosphaerina inaequalis*, TP+1006; (H) *Rectostipulina pentamerata*, TP+2301; (I) *Rectostipulina quadrata*, TP+0106; (J–K) *Rectocornuspira kalhori*, J, TP+2602, K, TP+4201; (L) *Reichelina* sp., TP+0509; (M–N) *Agathammina pusilla*, M, TP+0101, N，TP+0105; (O–P) *Globivalvulina bulloides*, O, TP+0516, P, TP+2607; (Q) *Neoendothyra permica*, TP-2003; (R) *Robuloides lens*, TP-0412; (S–T) *Glomomidiella nestellorum*, S, TP+0504, T, TP-1001; (U) *Sengoerina argandi*, TP-2005; (V) *Tolypammina* sp., TP+4203; (W) *Postendothyra tenuis*, TP-2008,

(X–Y) *Hemigordius* spp., X, TP-3026, Y, TP-4507; (Z) *Geinitzina uralica*, TP+2415; (a–b) *Ichthyofrondina palmata*, a, TP-2006, b， TP-3015; (c) *Pachyphloia robusta*, TP+0111; (d) *Pachyphloia schwageri*, TP+2410; (e) *Pachyphloia ovata*, TP+1010; and (f) *Nodosinelloides sagitta*, TP-2004. Sample numbers reflect position in cm above or below a zero datum in the sandy limestone bed. All scale bars are 0.1 mm in length.

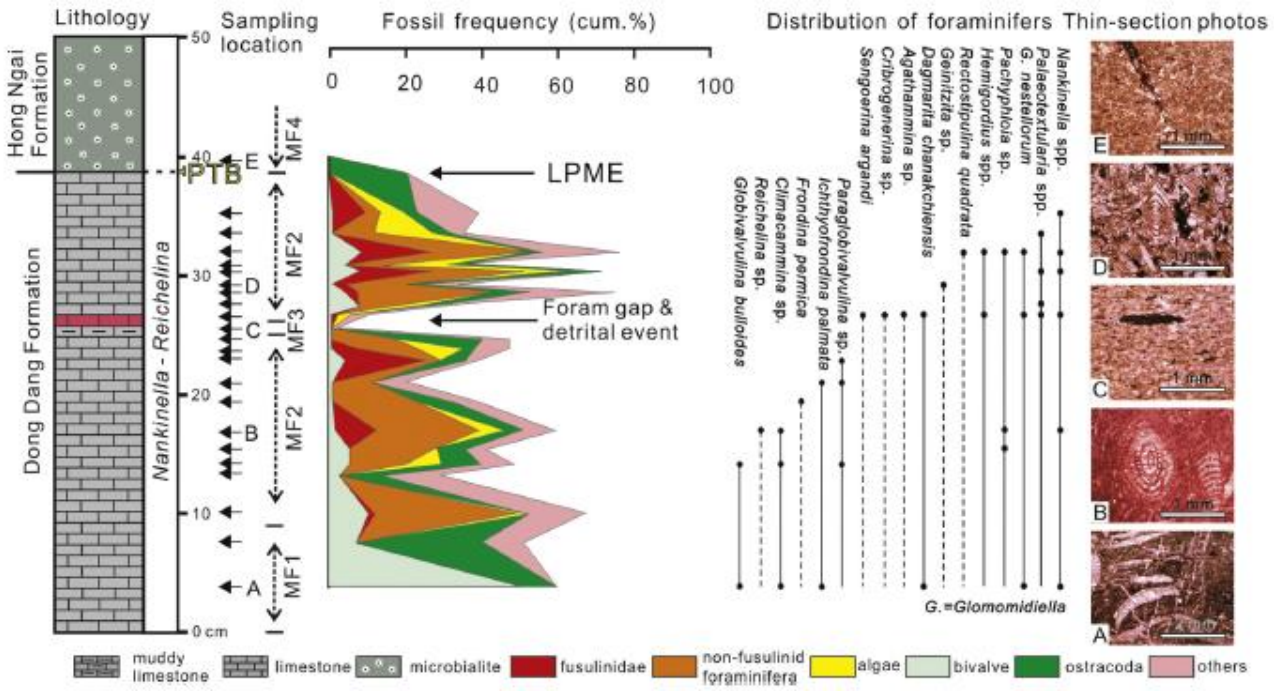

Fig. 9. Skeletal composition and foraminiferal distribution in the Lung Cam section. MF1: molluscan packstone; MF2: algal-foraminiferal packstone-grainstone; MF3: clast-bearing mudstone; MF4: dolomitized wackestone. Fossil frequency = fossil count / total count × 100 % (based on point-counting in thin sections).

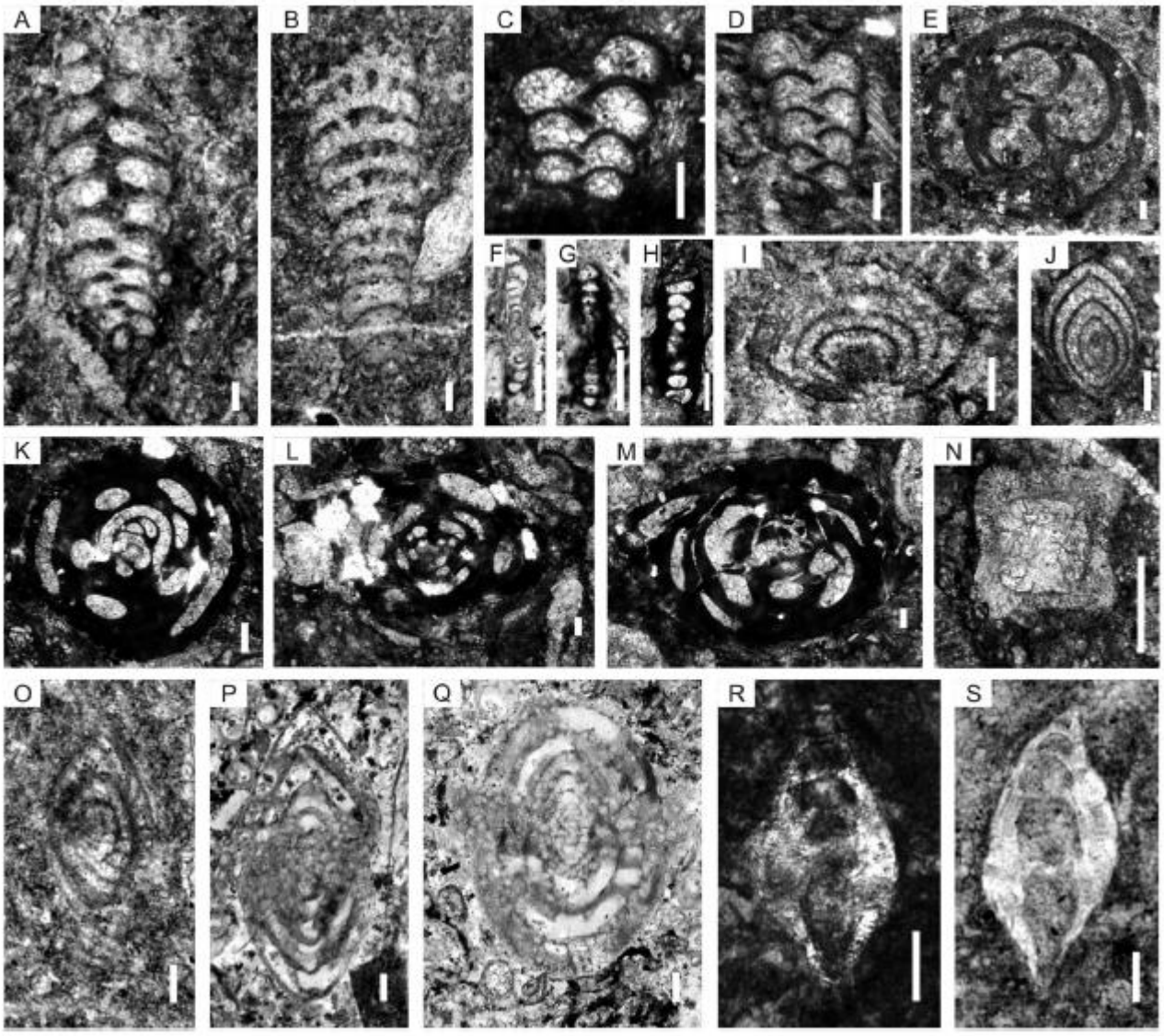

841

842 **Fig. 10.** Foraminifers of the Lung Cam section. (A) *Palaeotextularia* sp., LC0B02 (specimen
843 number); (B) *Climacammina* sp., LC17T07; (C–D) *Dagmarita chanakchiensis*, C, LC2B12; D,
844 LC2609; (E) *Paraglobivalvulina* sp., LC12B02; (F–H) *Hemigordius* spp., F, LC506, G, LC509, H,
845 LC806; (I–J) *Ichthyofrondina palmata*, I, LC12B03, J, LC2613; (K–M) *Glomomidiella nestellorum*,
846 K, LC817, L, LC802, M, LC803; (N) *Rectostipulina quadrata*, LC810; (O) *Reichelina* sp., LC17T09;
847 (P–Q) *Nankinella* spp., P, LC505, Q, LC510; and (R–S) *Pachyphloia* sp., R, LC17T06, S, LC19T02.
848 All scale bars are 0.1 mm in length.

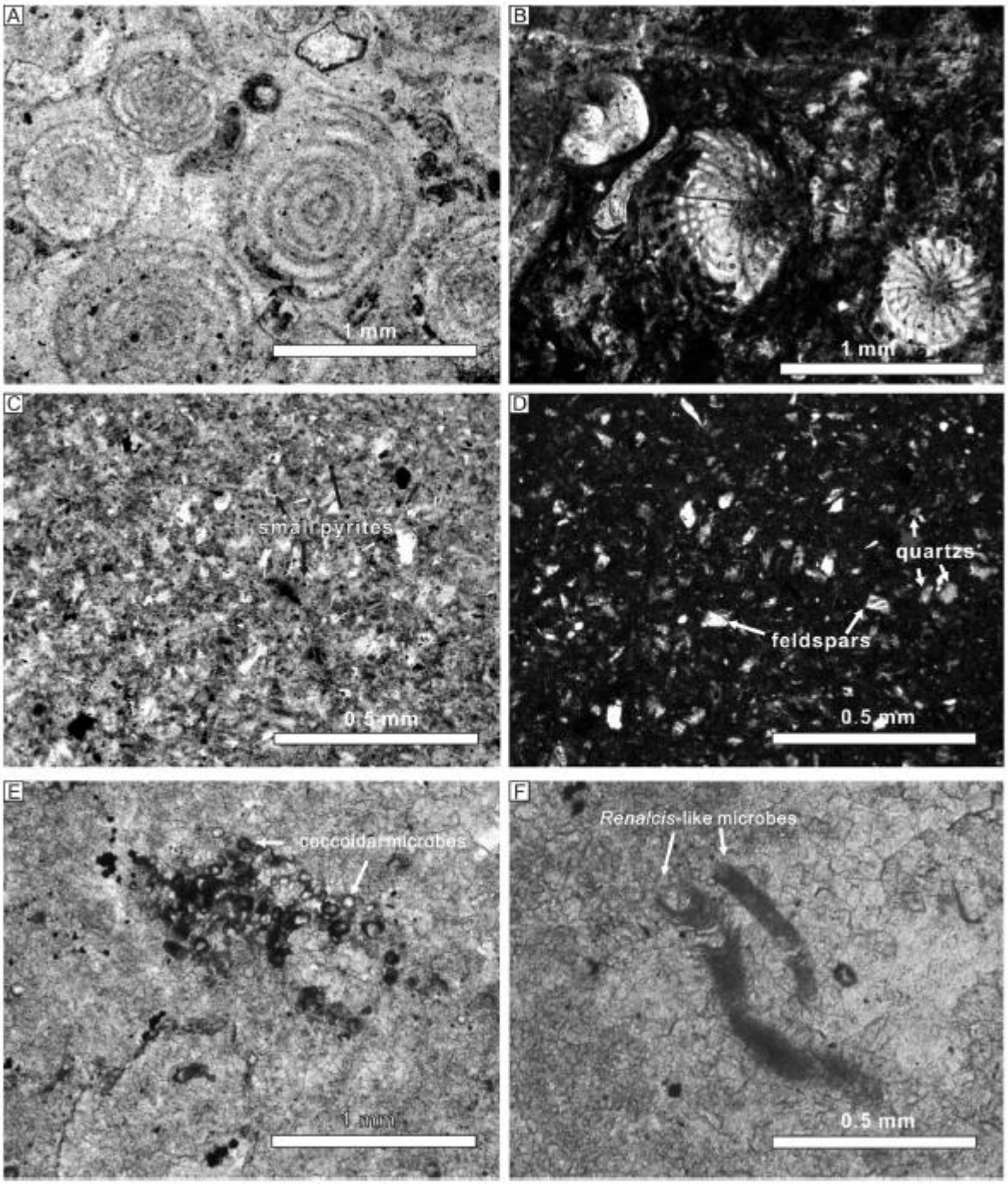

849

850 **Fig. 11.** Microfacies and minerals of the uppermost Permian carbonates. (A) Foraminiferal
851 grainstone (dominated by fusulinid skeletons) from the Wengna section, sample WN-14. (B)
852 Foraminiferal packstone (dominated by fusulinid skeletons) from the Taiping section, sample TP+2.1.
853 (C) Quartz and feldspar grains in sandy limestone from the Taiping section, sample TP-0.1. (D) Same
854 as C but in polarized light. (E) Cluster of coccoidal microbes from the Wengna section, sample

855 WN-20. (F) Lunate chambered micritic belts, interpreted as *Renalcis*-like microbes, from the Taiping

856 section, sample TP+3.2.

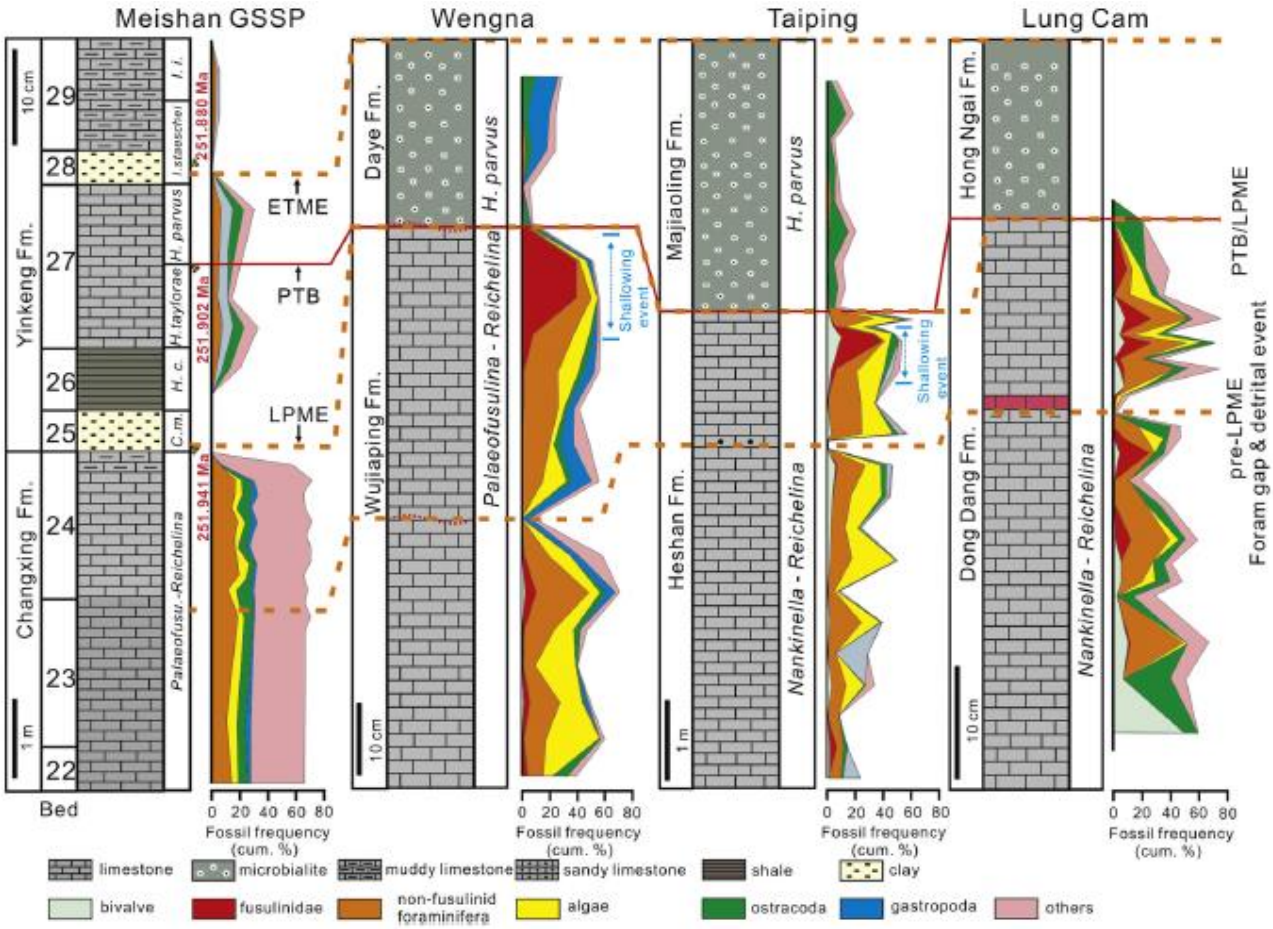

857

858 **Fig. 12.** Comparison of skeletal composition changes among the three study sections. LPME = latest

859 Permian mass extinction, PTB = Permian-Triassic Boundary, ETME = earliest Triassic mass

860 extinction. U-Pb radiometric dates are from Burgess et al. (2014). Skeletal composition data for

861 Meishan are from Kaiho et al. (2006) and Chen et al. (2015). Note change in vertical scale at

862 Meishan between the Changxing and Yinkeng formations.